**Content**

1. Response to referee #1
2. Response to referee #2
3. Revised manuscript
4. Changes with respect to previous version

We would like to thank referee #1 for his/her detailed comments on our manuscript. In the following, you will find our responses to each specific comment and technical correction addressed.

Specific comment (1): I recommend to rewrite the 'Introduction'. The section 'Introduction' must be more general. In the 'Introduction' there is no need for technical details and formulas. Technical details and formulas must be provided in the following section (see next point). Instead, provide a brief overview on the state of the art in tomography. Provide some relevant references, e.g. Bender et al., 2011, Champollion et al., 2005, Hirahara, 2000, and their findings. In all the above mentioned works bending effects were ignored. Therefore you should then provide references where bending effects are taken into account. Here you should mention Zus et al (2015) (not cited in the manuscript) and a paper that appeared two years later Aghajany and Amerian (2017) (cited in the manuscript).

Author's response: According to the reviewer's suggestion, we will restructure the first section of the manuscript as follows: The technical details and formulas will be shifted to a new section '3 The principles of GNSS tomography'. A paragraph about achievements in GNSS tomography will be added and all references suggested by the reviewer will be mentioned in the revised version of the manuscript.

Specific comment (2): Section 1 ('Introduction') and 2 ('Atmospheric bending effects in GNSS signal processing') need a complete makeover. I suggest to merge the two sections to one section with the following title 'Atmospheric bending effects and WV tomography'. To my understanding you are concerned with SWDs and not STDs. In short, I recommend the following structure for this section:

2.1 Atmospheric bending effects

Here you should at first introduce the basic observable, i.e., STDs. You can either use eq 2 or 10. They are essentially the same. I recommend to use eq 2. Hence, you start as follows: The STD is defined as (Bevis et al. 1992)

STD = int n ds – g

n...index of refraction s...arc length of bent ray-path (refer to section 3) g...geometric distance between satellite and station

Then, you introduce refractivity N. In essence

n=10*(-6) N + 1

and therefore

STD = int 10**(-6) N ds + s – g

Then you introduce the hydrostatic and wet refractivity

N= Nh + Nw

and therefore

STD = int 10**(-6) Nh ds + s – g + int 10**(-6) Nw ds

Next, you introduce the following quantities

SHD = int 10**(-6) Nh ds + s – g

and

SWD = int 10**(-6) Nw ds

such that

STD = SHD + SWD

At this point it is again important to mention that the ray-path (and therefore the arclength s) depends on the 'total' refractivity N (refer to section 3).

Then you claim that the SWD can be accurately estimated with the GNSS. In essence, you introduce the assembled STD that is used in the GNSS analysis (eq 11)

STD_GPS = ZHD_GPS * mh(e) + ZWD_GPS * mw(e) + mg(e) (N cos(a)+ E sin(a))

and provide the formula that you use to recover the SWD. I can only guess (please

provide the details) something like this

SWD_GPS = STD_GPS - ZHD_NWM * mh(e)

or better yet something like this

SWD_GPS = STD_GPS - ZHD_NWM * mh(e) - mg(e) (Nh_NWM cos(a)+ Eh_NWM*sin(a))

where ZHD_NWM is ZHD derived from a NWM (or derived from in situ pressure sensor) and Nh_NWM and Eh_NWM are the hydrostatic gradient components derived from a NWM. Here you can mention that the hydrostatic mf (which is derived under the assumption of a spherically layered troposphere) takes into account the geometric bending term. In essence,

mh = (int 10**(-6) Nh ds + s – g) / ZHD

With this details you are finished with 2.1 and prepared for 2.2

2.2 WV tomography

Since the observable you consider are SWDs, there is no need for eq 3 and 4. You can start directly with the following formula

SWD = int 10**(-6) Nw ds

and its numerical approximation

SWD _ sum_i 10**(-6) Nw_i ds_i

where you again explicitly mention that, because of ray-path bending, s does not equal g (refer to section 3). Then you can proceed with your eq 6 and 7. It is important that you explain what P and Pc is. I guess (please provide the details) that Pc tells us something about the uncertainty of the observations and P tells us something about the uncertainty of the a-prior (first-guess or background) wet refractivity?

With this you are finished with section 2 and proceed with your section 3.

Author's response: Thank you for your detailed suggestions. We agree that a restructure of the first two section can help to improve the understanding of our methods. In consequence, we will replace Eq. 10 by Eq. 2 and will derive the relations between STD, refractivity and bending from this equation in the way suggested by the reviewer. Since the focus of this paper lays on atmospheric bending effects, thereby we will not go into detail on how the SWD is obtained from GNSS signals but will show how and to what extend atmospheric bending is compensated in GNSS signal processing using the concept of mapping function - in particular for VMF1.

Instead of section '2.2 WV tomography' the manuscript will be extended by a new section '3 The principles of GNSS tomography'. This will include the basic equations of tomography, presented in a consistent way to section '2 Atmospheric bending effects in GNSS signal processing'. In addition, we will add a more detailed explanation of the singular value decomposition and weighting method applied, as requested by reviewer 2.

Specific comment (3): I suggest that somewhere in the manuscript you plot the following difference

dSWD = SWD_T - SWD_0

as a function of the elevation angle for some station. Here SWD_0 is the SWD calculated along the straight line path and SWD_T is the SWD calculated along the ray-path.

In essence,

dSWD = sum_i 10**(-6) Nw_i ds_i - sum_i 10**(-6) Nw_i dg_i

I guess you will find that the following inequality holds true for any elevation angle

SWD_0 > SWD_T

due to the fact that the ray-path traverses the troposphere at higher altitudes than the straight line path. This would imply that when ray-path bending is not taken into account in tomography the reconstructed troposphere is too dry. To see this you could chose some 'true' wet refractivity field, say N_w0, and simply replace in your eq 7 the term

(SWD - A*N_w0)

by dSWD. I strongly recommend to do this somewhere in the manuscript.

Author's response: In Figure 6 of the manuscript we plotted the additional ray paths caused by straight-line assumption and discussed its impact on the tomography results. As highlighted by the reviewer, it will lead to a drying effect in the reconstructed refractivity field. To provide some numbers, we computed the differences in SWD (dSWD = SWD_T – SWD_0) and the corresponding paths lengths within the voxel model as suggested by the reviewer for the 6 GNSS sites mentioned in Table 1. Therefore, we made use of the ALARO model data as 'true refractivity field' and ray-traced all lines-of-sight to the GNSS satellites in view, in total 720 observations distributed over 8 epochs (0, 3, 6 … UTC) on DoY 121, 2013. The resulting difference (dSWD) are always positive and up to 2.2 cm for ~5 degrees elevation angle. In addition, we computed the resulting drying effect in the refractivity field, which follows from the additional ray path:

dN1 = SWD_T[mm] * (ds_0 [km] - ds_T [km])

In addition, we computed the drying effect, caused by the fact, that the straight-line traverses the troposphere at lower altitudes (assuming exponential decrease of Nw with height between the model layers)

dN2 = (SWD_T[mm] – SWD_0[mm]) * ds_0 [km]

Both effects have to be taking into account when computing the drying effect in the reconstructed refractivity field obtained along the signal path if bending is not considered.

Author's changes in manuscript: In the revised version of the manuscript we will plot the additional paths lengths (Figure 6a) together with dN1 and dN2 as function of elevation angle (as Figure 6b and 6c) and will add a short description in the text how it was computed.

Technical corrections:

Abstract L7: '...Thereby, the ray-tracing approach itself but primarily the quality of the a prior field has a significant impact on the reconstruction quality...' improve the writing.

Author's response: This part of the Abstract will be rewritten as follows: 'Thereby, not only the ray-tracing method but also the quality of the a priori field has a significant impact on the quality of the tomography retrievals.'

Introduction L15: ’GNSS’ abbreviation not introduced here.

Author’s response: Abbreviation ‘GNSS’ will be spell out the first time when it is used in the manuscript as ‘Global Navigation Satellite Systems’

Section 3.1 L18: The inner loop you use is to solve the so called ’homing in problem’ (you make use of a shooting method). Please state this more clearly here.

Author’s response: In the revised manuscript, we will modify section 3.1 L16 ff as follows: ‘After setting the initial parameters, the 'true' ray path is reconstructed iteratively by making use of ray-tracing shooting techniques. Therefore, total refractivity derived from an a priori field is read in and pre-processed for ray-tracing. Hereby, the input data is interpolated vertically and horizontally to the vertical plane, spanned by the y- and z-axis.

In the ray-tracing loop, for each height layer $h_{i+1}$ with $i=1:(t-1)$ where $t$ defines the top layer of the voxel model, the geocentric coordinates and the corresponding angles are computed as follows: [..]

Section 3.1 L24: What is the ’outgoing’ elevation angle? Please provide a clear definition here.

Author’s response: The outgoing elevation angle is determined through the straight-line geometry between the satellite and entry-point of the signal into the atmosphere. In the revised version of the manuscript, we will call it ‘the vacuum elevation angle’ with reference to Figure 1.

Section 3.2 L4: ’...In consequence, the reconstructed...’. The phrase ’In consequence’ can be avoided here and at various other places.

Author’s response: The sentence ‘In consequence, the reconstructed signal travels significantly apart from the observed signal.’ will be removed and the entire manuscript will be revised accordingly.

Section 3.2.2: I suggest to show in Fig 4. directly the difference in SWD[m] and not the difference in the bending angle [arcsec]. Also, I do not find the formula for the bending angle in the manuscript. I guess you mean something like arcos(v1,v2) where v1 is the tangent unit vector of the ray-path at the satellite and v2 is the tangent unit vector of the ray-path at the station?

Author's response: The bending angle error in Figure 4 is the difference in elevation angle between full ray-tracing (until ~80 km altitude) and ray-tracing to the upper rim of the tomography model + bending model. Due to the distance of the satellite, it is widely consistent with the bending angle error obtained by analysis of the tangent unit vectors.

However, we agree that errors in bending angle are difficult to interpret. Thus, we will convert it into ray path errors and displacement, i.e. how much the ray entry-point differs due to errors in the bending model. We assume that this parameter is more of interest than SWD, since we would like to focus in this paper more on geometrical aspects and its impact on the tomography solution.

Section 4.1: I suggest to add in Fig 8. the difference for the a-prior (first guess or background) refractivity (ALARO). Is the radiosonde data assimilated into ALARO?

Author's response: This radiosonde data is not assimilated into ALARO. We will add the differences between radiosonde and ALARO to Figure 8 in the revised version of the manuscript.

References: Check all references carefully. For example,

Fritsche, M., Dietrich, R., Knofel, C., Rulke, A., and Vey, S.: Impact of higher-order ionospheric terms on GPS estimates, Geophys. Res. Lett., 32, 1–5, 2005.

Bender, M., Stosius, R., Zus, F., Dick, G., Wickert, J., Raabe, A. (2011): GNSS water vapour tomography – Expected improvements by combining GPS, GLONASS and Galileo observations. - Advances in Space Research, 47, 5, pp. 886âˇAˇ T897. DOI:http://doi.org/10.1016/j.asr.2010.09.011

In the manuscript the correct citation should be e.g. Böhm et al 2006 and not Böhm et al 2006a. Likewise the correct citation should be Hobiger et al 2008 and not Hobiger et al 2008a (there is no b).

Author's response: Thank you. The errors in the references will be corrected and carefully checked again before submission of the revised manuscript.

Additional Reference:

Zus, F., Dick, G., Heise, S. and Wickert, J.: A forward operator and its adjoint for GPS slant total delays, Radio Science, 50, 393– 405, doi: 10.1002/2014RS005584, 2015.'

Author’s response: Will be added to the revised version of the manuscript

We would like to thank referee #2 for his/her valuable suggestions. In the following, you will find our responses, separately for each comment/concern.

Comment: The paper outlines a method for including ray bending in GNSS tomography. My main concern relates to the iterative retrieval technique, and the possible confusion between "a priori" and "first guess".

Author's response: In the revised version of the manuscript, the terms "a priori" and "first guess" will be used according to its definition in 'Inverse Methods for Atmospheric Sounding Theory and Practice' by Clive Rogers, section 5.6.2 as "the best estimate of the state before the measurement is made" (a priori) and as 'the starting point of an iteration' (first guess).

Comment: Equation 7 should not be used in iterative form, and therefore a solution from eq. 7 should not be used as "a priori" for the next iteration (lines 7-8, page 7). This is covered in section 5.6.2 ("A popular mistake") in Inverse Methods for Atmospheric Sounding Theory and Practice by Clive Rogers. I suggest that this issue should be clarified before moving to the discussion phase, because it impacts all of the results.

Author's response: We agree, by using the result of a previous iteration as first guess for the next iteration provides in a least squares sense not an optimal estimation. In consequence, we adapted our approach slightly – following the non-linear iterative approach suggested by Iyer and Hirahara, Seismic tomography: Theory and practice, 1993. Therefore, we keep the initial a priori field as first guess for each iteration but use the result of each iteration for improving the reconstruction of the signal paths. Therewith, and according to Fermat's principle (first order changes of the ray path lead to second order changes in travel time) the estimation error can be significantly reduced. Besides, the aim should be always to make use of the best available a priori field, especially if low elevation observations are involved. If this is not possible, the proposed non-linear iterative approach will allow for a more exact reconstruction of the signal paths, even if the used a priori refractivity field deviates significantly from the true atmospheric conditions.

Author's changes in manuscript: Due to the adaption in the tomography approach, several parts of the manuscript will be revised. This includes:

Section 3.2.1 The a priori refractivity field, page 7 line 7-14,

Section 4 Impact of atmospheric bending on the tomography solution, page 10 line 12-22,

Section 4.1 Validation with radiosonde data, page 12 line 1-3,

Section 5 Conclusions, page 12 line 6-7, page 13 line 4-7 and line 16-18 and

Figure 3, 7 and 8.

Minor points

Comment: I do not understand why the authors use singular value decomposition in Eq. 7. Normal matrix inversion should suffice.

Author's response: Solving Eq. (6) for Nw requires the inversion of matrix A. In GNSS tomography, matrix A is mostly singular; in consequence, a straightforward inversion is not possible. Thus, for our solution we make use of singular value decomposition methods for solving the ill-posed inversion problem. Together with a proper singular value selection method like L-curve technique (see Moeller, 2017), it allows for solving the equation system and for retrieving as much signal as possible from the observations without introducing too large artefacts.

Author's changes in manuscript: We will add a more detailed explanation of our approach, in particular why we used SVD, to the revised version of the manuscript below Eq. 7.

Comment: The meaning of the weighting matrices should explained (they are the inverse of covariance matrices I think) and they should be clearly defined.

Author's response: The weighting matrices P and Pc are the inverse of the variance-covariance matrices C and Cc. They are defined separately for the SWDs, i.e. the observations (C) and the first guess (Cc). The diagonal elements of C were computed as function of elevation angle: sin(e)^2*sig_ZTD^2, whereby sig_ZTD = 2.5 mm reflects the accuracy of the estimated zenith total delays. The diagonal elements of Cc were derived from a weighting model based on height-dependent error curves for pressure, temperature and specific humidity in form of standard deviations (see Steiner A. K. et al., Error characteristics of refractivity profiles retrieved from CHAMP radio occultation data, 2006). Both error matrices were introduced into the tomography solution for proper weighting of the individual observations against the first guess.

Author's changes in manuscript: An explanation of the weighting method will be added to Chapter 1 after Eq. 7.

Comment: The work might benefit from investigating how ray-bending is handled in GPS radio occultation measurements. EG, Burrows, C. P., Healy, S. B., and Culverwell, I. D.: Improving the bias characteristics of the ROPP refractivity and bending angle operators, Atmos. Meas. Tech., 7, 3445-3458, https://doi.org/10.5194/amt-7-3445-2014, 2014.

Author's response: According to the reviewer's suggestion, we did a literature study on ray-tracing methods, in particular for assimilation of radio occultation measurements into numerical weather prediction systems.

While wave-theoretic approaches can help to increase the vertical resolution of the refractivity profile derived from radio occultation measurements, nowadays approaches based on the principles of geometric optics are still valid for operational analysis of radio occultation measurements. The main reason is that necessary assumption in signal processing, like the symmetric assumption or limitations in the GPS signal structure are still the dominating factors (Melbourne W. G., Radio Occultation Using Earth

Satellites: A Wave Theory Treatment, 2004). Thus, and for highest consistency, also ray-tracing approaches based on the principles of geometric optics are widely used for reconstruction of the signal geometry, especially for assimilation of radio occultation measurements.

In contrast to radio occultation, the analysis of ground-based observations, including the weighting of ground-based observations in GNSS data processing, is based on different geometrical parameters. While in radio occultation, the bending angle is described as function of impact parameter a, for ground-based observations, elevation and azimuth angle are used for characterizing the observation geometry. In consequence, the optimal ray-tracing approach for ground-based observation and its conversion differs from approaches used for radio occultation measurements.

Nevertheless, in both cases the quality of the a priori field, but also how refractivity is interpolated between the given model levels, will have an impact on the ray-traced signal paths. Latter is clearly shown in the paper of Burrows C. P. et al. (2014), as suggested by the reviewer.

In the best case, the interpolation between model levels is carried out on state parameter level, i.e. separately for pressure, temperature and water vapour pressure as obtained from the a priori field. However, since this approach is not applicable in iterative tomography processing, we assume exponentially varying refractivity. We are aware, that thereby the bending angle is slightly underdetermined. Nevertheless, in relation to the total bending effect, its contribution is fractional. Thus, we will not further modify our ray-tracing approach but we will address this affect in section '5 Conclusions'.

Author’s changes in manuscript: In the manuscript, we will add a brief review of existing ray-tracing approaches in section ‘3 Reconstruction of GNSS signal paths’ and will highlight the differences between radio occultation and ground-based observations and its consequences on the ray-tracing approach. Furthermore, we will add a paragraph to section ‘5 Conclusion’ to address the interpolation problem in the iterative non-linear tomography approach to highlight its impact on the tomography solution.

# Atmospheric bending effects in GNSS tomography

Gregor Möller[1] and Daniel Landskron[1]

[1]Department of Geodesy and Geoinformation, Vienna University of Technology, Vienna, Austria

**Correspondence:** Gregor Möller (gregor.moeller@tuwien.ac.at)

**Abstract.** In GNSS tomography, precise information about the tropospheric water vapor distribution is derived from integral measurements like ground-based GNSS slant wet delays (SWDs). Therefore, the functional relation between observations and unknowns, i.e. the signal paths through the atmosphere have to be accurately known for each station-satellite pair involved. For GNSS signals observed above 15 degrees elevation angle, the signal path is well approximated by a straight line. However, since electromagnetic waves are prone to atmospheric bending effects, this assumption is not sufficient anymore for lower elevation angles. Thus, in the following, a mixed 2D piecewise linear ray-tracing approach is introduced and possible error sources in reconstruction of the bended signal paths are analyzed in more detail. Especially, if low elevation observations are considered, unmodeled bending effects can introduce a systematic error of up to $10-20ppm$, on average of $1-2ppm$ into the tomography solution. Thereby, not only the ray-tracing method but also the quality of the a priori field can have a significant impact on the reconstructed signal paths, if not reduced by iterative processing. In order to keep the processing time within acceptable limits, a bending model is applied for the upper part of the neutral atmosphere. It helps to reduce the number of processing steps by up to $85\%$ without significant degradation in accuracy. Therewith, the developed mixed ray-tracing approach allows not only for a correct treatment of low elevation observations but is also fast and applicable for near real-time applications.

## 1 Introduction

For conversion of precise integral measurements into two- or three-dimensional structures, a technique called tomography has been invented. In the field of GNSS meteorology, the principle of tomography became applicable with the increasing number of Global Navigation Satellite System (GNSS) satellites and the build-up of densified ground-based GNSS networks in the 1990s (Raymond et al., 1994; Flores Jimenez, 1999). Since then, a variety of tomography approaches based on raw GNSS phase measurements (Nilsson, 2005), double difference residuals (Kruse, 2001), slant delays (Flores Jimenez, 1999; Hirahara, 2000) or slant integrated water vapor (Champollion et al., 2005) has been developed for the accurate reconstruction of the water vapor distribution in the lower atmosphere. An overview about the major developments within this field of research since Flores Jimenez (1999) is provided by Manning (2013).

While in most tomography approaches, observations gathered at low elevation angles are discarded (Bender et al., 2011; Champollion et al., 2005; Hirahara, 2000), straight line signal path reconstruction is sufficient for the determination of the path lengths. However, Bender and Raabe (2007) showed that especially low elevation observations can be a very useful source of information in GNSS tomography. Besides their information content about the lower troposphere, the additional observations strengthen the observation geometry and therewith, contribute to a more reliable tomography solution. However, a correct treatment of low elevation observations requires more advanced ray-tracing algorithms. The first paper which deals with bended ray path reconstruction in GNSS tomography was published by Zus et al. (2015), with main focus on the reconstruction of the signal paths for delay estimation but also for assimilation of GNSS slant delays into numerical weather prediction systems. Most recently, Aghajany and Amerian (2017) published their results about 3D ray-tracing in water vapor tomography and briefly analyzed its impact on the tomography solution.

Based on the existing studies, in the following, a more detailed discussion of possible error sources in signal path reconstruction is provided. Therefore, Sect. 2 describes the effect of atmospheric bending and its handling in GNSS signal processing. Section 3 describes the principles of GNSS tomography and how the basic equation of tomography is solved for wet refractivity. Section 4 introduces the concept for reconstruction of signal paths using ray-tracing techniques. Hereby, the modified piecewise linear ray-tracing approach is described - including its ability for reconstruction of the GNSS signal geometry. In Sect. 5, the defined ray-tracing approach is applied to real SWDs and its impact on the tomography solution is assessed and validated against radiosonde data. Section 6 concludes the major findings.

## 2 Atmospheric bending effects in GNSS signal processing

The effect of atmospheric bending on GNSS signals is related to the propagation properties of electromagnetic waves. In vacuum, GNSS signals travel with the velocity of light. When entering into the atmosphere, the electromagnetic wave velocity changes, dependent on the electric permittivity ($\epsilon$) and magnetic permeability ($\mu$) of the atmospheric constituents and the frequency of the electromagnetic wave. The ratio between the velocity of light $c$ in vacuum and the velocity $\nu$ in a medium defines the refractive index $n$.

$$n = \frac{c}{\nu} = \sqrt{\frac{\epsilon \cdot \mu}{\epsilon_0 \cdot \mu_0}} \tag{1}$$

For signals in the microwave frequency-band, $n$ ranges from 0.9996 to 1.0004. Thus, $n$ is usually replaced by refractivity $N$, expressed in mm/km (ppm).

$$N = 10^6 \cdot (n - 1) \tag{2}$$

The GNSS signal delay in the lower atmosphere, also known as slant total delay ($STD$), is related to refractivity by the following equation (Bevis et al., 1992):

$$STD = 10^{-6} \cdot \int\limits_R N \cdot ds + \left[ \int\limits_R ds - \int\limits_S ds \right] \tag{3}$$

The first term of Eq. (3) describes the change in travel time due to velocity changes along the true ray path R. The second term (about three orders of magnitude smaller than the first term) is related to the difference in geometrical path length between the true (R) and the chord signal path (S). According to Dalton's law, the refractivity of air can be split up into a hydrostatic and a wet component: $N = N_h + N_w$. Therewith, the GNSS signal delay reads:

$$STD = SHD + SWD = 10^{-6} \cdot \int\limits_R N_h \cdot ds + 10^{-6} \cdot \int\limits_R N_w \cdot ds + \left[ \int\limits_R ds - \int\limits_S ds \right]. \quad (4)$$

The slant wet delay $(SWD)$ depends on the wet refractivity along the true ray path $R$.

$$SWD = 10^{-6} \cdot \int\limits_R N_w \cdot ds \quad (5)$$

The slant hydrostatic delay $(SHD)$ results from the the hydrostatic refractivity along $R$ and, by definition, from the additional path length due to atmospheric bending.

$$SHD = 10^{-6} \cdot \int\limits_R N_h \cdot ds + \left[ \int\limits_R ds - \int\limits_S ds \right] \quad (6)$$

While signal path $S$ follows from the straight line geometry between satellite and receiver, the true signal path $R$ depends in addition on the hydrostatic and the wet refractivity distribution along the signal path (see Sect. 3 for more details).

In GNSS signal processing, the integral along the signal path is usually replaced by the zenith delay and a mapping function. Therefore, Eq. (4) is rewritten as follows:

$$STD(\varepsilon, \alpha) = SHD + SWD = ZHD \cdot mf_h(\varepsilon) + ZWD \cdot mf_w(\varepsilon) + G(\varepsilon, \alpha) \quad (7)$$

where $ZHD$ is the zenith hydrostatic delay, $ZWD$ is the zenith wet delay and $mf_h$ and $mf_w$ are the corresponding mapping functions, which describe the elevation ($\varepsilon$) dependency of the signal delay. The elevation and azimuth $(\alpha)$ dependent first-order horizontally asymmetric term $G(\varepsilon, \alpha)$ reflects local variations in the atmospheric conditions: see MacMillan (1995), Chen and Herring (1997) or Landskron and Böhm (2018). In practice, e.g. when using VMF1 mapping function (Böhm et al., 2006) or similar mapping concepts, the tropospheric delay due to atmospheric bending is absorbed by the hydrostatic mapping function term $mf_h$. Comparisons between ray-traced $SHD(\varepsilon)$ and 'mapped' $SHD(\varepsilon) = ZHD \cdot mf_h(\varepsilon)$ slant hydrostatic delays reveal that about 97 % of the atmospheric bending effect is compensated by the VMF1 hydrostatic mapping function (see Appx. A for further details).

## 3 The principles of GNSS tomography

According to Iyer and Hirahara (1993), the general principle of tomography is described as follows:

$$f_s = \int\limits_R g_s \cdot ds \quad (8)$$

where $f_s$ is the projection function, $g_s$ is the object property function and $ds$ is a small element of the ray path $R$ along which the integration takes place. In GNSS tomography, $g_s$ is usually replaced by wet refractivity $N_w$, and integral measure $f_s$ by $SWD$ (the prefactor of $10^6$ vanishes if $ds$ is provided in kilometer and $SWD$ in millimeter).

$$SWD = \int\limits_R N_w \cdot ds \quad (9)$$

A full non-linear solution of Eq. (9) for wet refractivity is not of practical relevance since according to Fermat´s principle, first order changes of the ray path lead to second order changes in travel time. In consequence, by ignoring the path dependency in the inversion of $N_w$ along $ds$ and by assuming the ray path as a straight line, a linear tomography approach can be defined which is well applicable to $SWDs$ above 15 degrees elevation angle (Möller, 2017). However, with decreasing elevation angle, the true signal path deviates significantly from a straight line. In consequence, by ignoring atmospheric bending, a systematic error is introduced in the tomography solution. In order to overcome this limitation, in the following an *iterative tomography approach* is defined in which the bended signal path is approximated by small line segments. Similar to the linear tomography approach, thereby the neutral atmosphere or parts of it are discretized in volume elements (voxels) in which the refractivity $N_{w,k}$ in each voxel $k$ is assumed as constant. Consequently, Eq. (9) can be replaced by:

$$SWD = \sum_{k=1}^{m} N_{w,k} \cdot d_k \tag{10}$$

where $d_k$ is the travelled distance in each voxel. Assuming $l$ observations and $m$ voxels, a linear equation system can be set up. In matrix notation it reads:

$$\boldsymbol{SWD} = \boldsymbol{A} \cdot \boldsymbol{N_w} \tag{11}$$

where $\boldsymbol{SWD}$ is the observation vector of size $(l,1)$, $\boldsymbol{N_w}$ is the vector of unknowns of size $(m,1)$ and $\boldsymbol{A}$ is a matrix of size $(l,m)$ which contains the partial derivatives of the slant wet delays with respect to the unknowns, i.e. the travelled distances $d_k$ in each voxel.

$$\boldsymbol{A} = \begin{bmatrix} \frac{\delta SWD_1}{\delta N_{w,1}} & \cdots & \frac{\delta SWD_1}{\delta N_{w,m}} \\ \vdots & \ddots & \vdots \\ \frac{\delta SWD_l}{\delta N_{w,1}} & \cdots & \frac{\delta SWD_l}{\delta N_{w,m}} \end{bmatrix} \tag{12}$$

Solving Eq. (11) for $\boldsymbol{N_w}$ requires the inversion of matrix $\boldsymbol{A}$.

$$\boldsymbol{N_w} = \boldsymbol{A^{-1}} \cdot \boldsymbol{SWD} \tag{13}$$

The inverse $\boldsymbol{A^{-1}}$ exists if $\boldsymbol{A}$ is squared and if the determinant of $\boldsymbol{A}$ is non-zero, otherwise matrix $\boldsymbol{A}$ is called singular. Unfortunately, singularity appears in GNSS tomography in most cases since the observation data is 'incomplete' and matrix $\boldsymbol{A}$ is not of full rank. Therewith, Eq. (13) becomes ill-posed, i.e. not uniquely solvable. In order to find a solution which preserves most properties of an inverse, in the following matrix $\boldsymbol{A}$ is replaced by pseudo inverse $\boldsymbol{A^+}$. According to Hansen (2000) the pseudo inverse is defined as follows:

$$\boldsymbol{A^+} = \boldsymbol{V} \cdot \boldsymbol{S^{-1}} \cdot \boldsymbol{U^T} \tag{14}$$

where U and V are orthogonal, normalized left and right singular vectors of A and matrix S is a diagonal matrix, which contains the singular values in descending order. In case a priori information $(\boldsymbol{N_{w0}})$ can be made available, it enters the tomography solution as first guess as follows:

$$\boldsymbol{N_w} = \boldsymbol{N_{w0}} + \boldsymbol{V} \cdot \boldsymbol{S}^{-1} \cdot \boldsymbol{U}^T \cdot \boldsymbol{A}^T \cdot \boldsymbol{P} \cdot (\boldsymbol{SWD} - \boldsymbol{A} \cdot \boldsymbol{N_{w0}}) \tag{15}$$

where matrix $\boldsymbol{U}$, $\boldsymbol{V}$ and $\boldsymbol{S}$ are obtained by singular value decomposition of matrix $\boldsymbol{A}^T \cdot \boldsymbol{P} \cdot \boldsymbol{A} + \boldsymbol{P_c}$. The weighting matrices $\boldsymbol{P}$ and $\boldsymbol{P_c}$ are defined as the inverse of the variance-covariance matrix $\boldsymbol{C}$ for the observations and $\boldsymbol{C_c}$ for the first guess, respectively. Assuming, that the observations are uncorrelated, the non-diagonal elements of $\boldsymbol{C}$ and $\boldsymbol{C_c}$ are zero and the diagonal elements are defined as follows:

$$\sigma_C^2 = \sin^2 \varepsilon \cdot \sigma_{ZWD}^2 \tag{16}$$

$$\sigma_{C_c}^2 = \left(\frac{\partial N_w}{\partial T} \cdot \sigma_T\right)^2 + \left(\frac{\partial N_w}{\partial q} \cdot \sigma_q\right)^2 + \left(\frac{\partial N_w}{\partial p} \cdot \sigma_p\right)^2 \tag{17}$$

whereby $\sigma_{ZWD} = 2.5mm$ reflects the uncertainty of the $ZWD$. The values for $\sigma_T$, $\sigma_q$ and $\sigma_p$ were taken from height-dependent error curves for pressure $(p)$, temperature $(T)$ and specific humidity $(q)$ as provided by Steiner et al. (2006) for the ECMWF (European Centre for Medium-Range Weather Forecasts) analysis data. For further details, the reader is referred to Möller (2017).

## 4 Reconstruction of GNSS signal paths

Assuming that the geometrical optics approximation is valid and that the atmospheric conditions change only inappreciably within one wavelength, the signal path is well reconstructible by means of ray-tracing shooting techniques (Hofmeister, 2016; Nievinski, 2009). Thereby, the basic equation for ray-tracing, the so-called Eikonal equation, has to be solved for obtaining optical path length $L$.

$$||\nabla L||^2 = n(\boldsymbol{r})^2 \tag{18}$$

From Eq. (18), a number of 3D and 2D ray-tracing approaches have been derived for the reconstruction of ground-based and space-based GNSS measurements and of their signal paths through the atmosphere (Hobiger et al., 2008; Zou et al., 1999).

The main difference between both observation types is related to the observation geometry. While for space-based GNSS observations derived in limb sounding, the bending angle is usually described as function of impact parameter $a$, for ground-based observations elevation and azimuth angle are used for characterizing the signal geometry. In consequence, the optimal ray-tracing approach will be significantly different for various observation geometries.

In order to find an optimal approach for operational analysis of ground-based measurements, Hofmeister (2016) carried out a number of exploratory comparisons. Based on the outcome, the 2D piecewise linear ray-tracer was defined as the optimal reconstruction tool for the iterative reconstruction of the atmospheric signal delays including atmospheric bending. It is limited to positive elevation angles but it is fast and almost as accurate as the 3D ray-tracer. However, for the use in GNSS tomography, the ray-tracing approach had to be further modified. In the following, the developed ray-tracing approach but also its impact on the GNSS tomography solution are discussed in more detail.

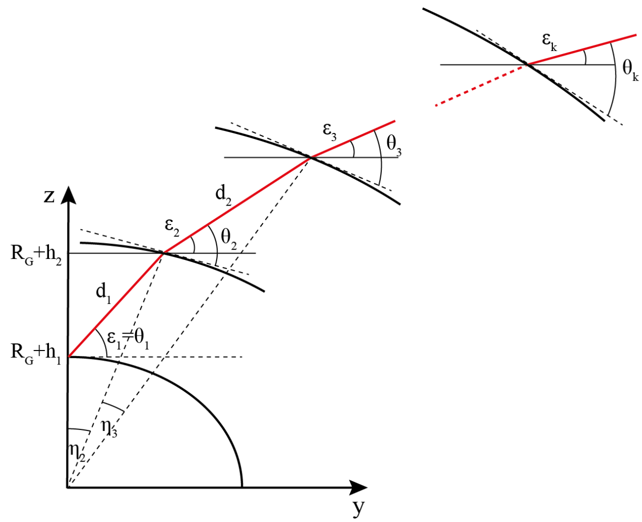


**Figure 1.** Geometry of the ray-tracing approach with the geocentric coordinates (y, z), the geocentric angles $(\eta, \theta)$, elevation angle $\varepsilon$ and $d$ as the distance between two consecutive ray points

### 4.1 Piecewise linear ray-tracer

The starting point for the 2D piecewise linear ray-tracer is the receiver position in ellipsoidal coordinates $(\varphi_1, \lambda_1, h_1)$, the 'vacuum' elevation angle $\varepsilon_k$ (see Fig. 1) and the azimuth angle $\alpha$ under which the satellite is observed. In case of GNSS tomography, these parameters can be determined with sufficient accuracy from satellite ephemerides and the receiver position - assuming straight line geometry. Therewith, the initial parameters for ray-tracing (see Fig. 1), i.e. the geocentric coordinates $(y_1, z_1)$ and the corresponding geocentric angles $(\eta_1, \theta_1)$ read:

$$y_1 = 0 \tag{19}$$

$$z_1 = R_G + h_1 \tag{20}$$

$$\eta_1 = 0 \tag{21}$$

$$\theta_1 = \varepsilon_k \tag{22}$$

where $R_G$ is the Gaussian radius, an adequate approximation of the Earth radius

$$R_G = \frac{a^2 \cdot b}{(a \cdot \cos\varphi_1)^2 + (b \cdot \sin\varphi_1)^2} \tag{23}$$

with $a$ and $b$ as the semi-axes of the reference ellipsoid (e.g. GRS80). The z-axis connects the geocenter with the starting point, the y-axis is defined perpendicular to the z-axis in direction (azimuth angle) of the GNSS satellite in view. After setting the initial parameters, the 'true' ray path is reconstructed iteratively by making use of ray-tracing shooting techniques. Therefore, total refractivity derived from an a priori field is read in and pre-processed for ray-tracing. Hereby, the input data is interpolated vertically and horizontally to the vertical plane, spanned by the y- and z-axis.

In the *ray-tracing loop*, for each height layer $h_{i+1}$ with $i = 1:(t-1)$ whereby $t$ defines the top layer of the voxel model, the geocentric coordinates and the corresponding angles are computed as follows:

$$y_{i+1} = y_i + d_i \cdot \cos\varepsilon_i \tag{24}$$

$$z_{i+1} = z_i + d_i \cdot \sin\varepsilon_i \tag{25}$$

$$\eta_{i+1} = \arctan\frac{y_{i+1}}{z_{i+1}} \tag{26}$$

$$\theta_{i+1} = \arccos\left(\frac{n_i}{n_{i+1}} \cdot \cos(\theta_i + \eta_{i+1} - \eta_i)\right) \tag{27}$$

$$d_i = -(R_G + h_i) \cdot \sin\theta_i + \sqrt{(R_G + h_{i+1})^2 - (R_G + h_i)^2 \cdot \cos^2\theta_i} \tag{28}$$

$$\varepsilon_{i+1} = \theta_{i+1} - \eta_{i+1} \tag{29}$$

where $d_i$ is the reconstructed path length between height layer $h_i$ and $h_{i+1}$ $(h_{i+1} > h_i)$. It depends on the observation geometry but also on the atmospheric conditions (refractive indices $n_i$ and $n_{i+1}$). By default, for our analysis, the spacing between two height layers $h_i$ and $h_{i+1}$ was set to 5 m, which corresponds to a maximum path length $d_i$ of 100 m - assuming an elevation angle of 3° ($5m/sin3°$).

The ray-tracing loop stops when the ray reaches the top layer $t$ of the voxel model. Assuming spherical trigonometry, the spherical coordinates $(\varphi_{i+1}, \lambda_{i+1})$ of the ray path segments follow by Eqs. (24) and (25) to:

$$\varphi_{i+1} = \arcsin\left(\sin\varphi_1 \cdot \cos(\eta_{i+1} - \eta_1) + \cos\varphi_1 \cdot \sin(\eta_{i+1} - \eta_1) \cdot \cos\alpha\right) \tag{30}$$

$$\lambda_{i+1} = \lambda_1 + \arctan\left(\frac{\sin\alpha}{\cot(\eta_{i+1} - \eta_1) \cdot \cos\varphi_1 - \sin\varphi_1 \cdot \cos\alpha}\right) \tag{31}$$

where $\varphi_{i+1}$ and $\lambda_{i+1}$ are defined in the range $[-\pi/2, \pi/2]$ and $[-\pi, \pi]$, respectively. The ray coordinates are necessary for interpolation of the refractive indices $n_i$ and $n_{i+1}$ for the next processing step $i$ but also for computation of the intersection points with the voxel model boundaries.

The ray-tracing loop is repeated until $\varepsilon_t - \varepsilon_k + g_{bend}$ is smaller than a predefined threshold (e.g. $10^{-6}$ degrees). While the elevation angle $\varepsilon_t$ is obtained by Eq. (29) for $i = t-1$, the correction term $g_{bend}$ accounts for the additional bending above the voxel model. Since atmosphere is almost in state of hydrostatic equilibrium, $g_{bend}$ can be well approximated by a bending model, like the one of Hobiger et al. (2008):

$$g_{bend}[°] = \frac{0.02 \cdot \exp^{\frac{-h}{6000}}}{\tan\varepsilon_k} \tag{32}$$

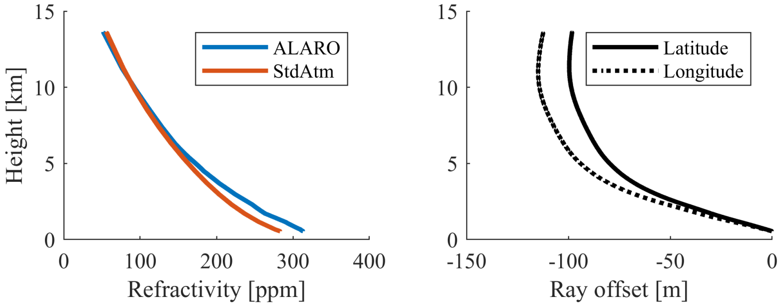


**Figure 2.** Ray-traced signal path differences (right) caused by differences in the a priori refractivity field (left)

where $h$ is replaced by $h_t$, the height of the voxel top layer. After convergence of the ray-tracing loop, the path length in each voxel is obtained by summing up the distances $d_i$ in each voxel. Thereby, allocation of the ray parts is carried out by comparison of the ray coordinates $(\varphi_i, \lambda_i, h_i)$ with the coordinates of the voxel model. The obtained ray paths in each voxel - for each station and each satellite in view - are used for setting up design matrix $\boldsymbol{A}$ (see Eq. 12).

## 4.2 Quality of reconstructed ray paths

### 4.2.1 The refractivity field

The quality of the ray-traced signal paths depends primarily on the quality of the refractivity field. Especially if no good a priori data can be made available, e.g. if standard atmosphere (StdAtm) is used instead of numerical weather model data (ALARO), the reconstructed signal path might deviate significantly from the 'true' signal path.

Figure 2 shows the impact of the refractivity field on the signal geometry, exemplary for a GNSS signal observed at station Jenbach, Austria $(\varphi = 47.4°, \lambda = 11.8°, h = 545m)$ with $\varepsilon = 5°$ and $\alpha = 230°$. At this particular epoch (May 4, 2013, 15 UTC), standard atmosphere deviates by about 30 ppm from the ALARO model data. Assuming ALARO as reference, ray-tracing through standard atmosphere causes a ray deviation of 100-200 m (see Fig. 2, right).

In order to reduce the impact of possible refractivity errors on the reconstructed ray paths and in further consequence on the tomography solution, ray-tracing was carried out iteratively. Therefore, the refractivity field obtained from the first tomography solution replaces the initial refractivity field for ray-tracing for the next iteration and so on. The processing is repeated until $\boldsymbol{N_w}$ converges.

Figure 3 (left) shows the convergence behavior assuming standard atmosphere (StdAtm) and ALARO model data as input. In both cases, the standard deviation of the differences in path length between two consecutive epochs ( $d_{k,i+1} - d_{k,i}$) was selected as convergence criteria. Both solutions converge after two iterations. Thereby, the path lengths within each voxel 'improve' by about $22m$ in case of standard atmosphere and by $11m$ in case of ALARO data. This result was expected, since ALARO data are closer to the 'true' atomospheric conditions. By comparison of Figure 3 (right) with Figure 2 (right) it is clearly visible,

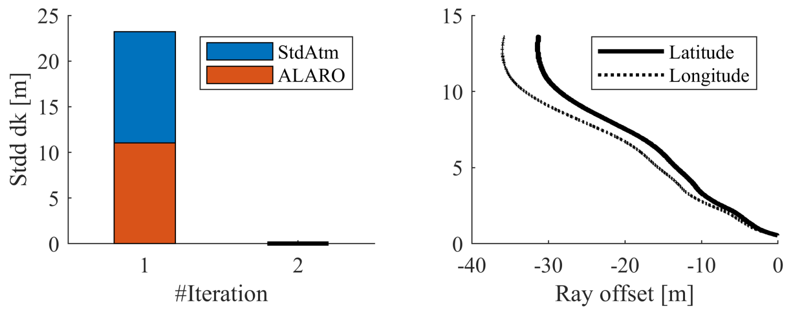


**Figure 3.** Convergence behavior (left) and ray-traced signal path differences after convergence (right). All iterations are based on the same first guess (standard atmosphere or ALARO numerical weather model data) but differ with respect to the refractivity field used for reconstruction of the bended signal paths

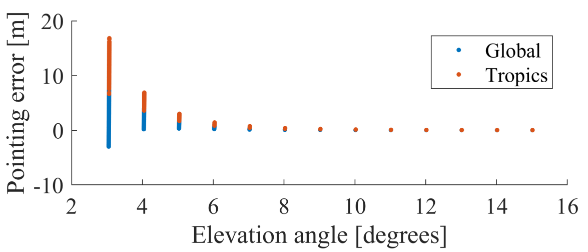


**Figure 4.** Point error at voxel model top $(h = 13.6km)$ caused by the bending model of Hobiger et al. (2008) - computed on a global $10°x10°$ grid over the period of one year, 2014 by comparison with ray-traced bending angles based on ECMWF analysis data

that the two additional iterations help to reduce the ray offset caused by errors in the standard atmosphere from $100-200m$ to $30-40m$. In Sect. 5 the resulting effect on the tomography solution is assessed.

#### 4.2.2 The empirical ray-bending model

Besides the refractivity field, the quality of the reconstructed ray paths might be also affected by errors in the bending model as defined by Eq. (32). Comparisons of the bending model with ray-traced bending angles on a global $10°x10°$ grid over the period of one year reveal that the error in bending is usually kept below 0.8 arcsec. Assuming a GNSS site near sea-level and an elevation angle of $5°$, an error in bending angle of $\pm 0.8$ arcsec causes an error in path length of up to $\pm 10m$, i.e. the reconstructed GNSS signal enters the voxel model slightly earlier or later than the observed GNSS signal. In Fig. 4, the bending error is visualized as pointing error at voxel model top. However, for the tomography solution this effect is too small to be significant. Thus, it can be concluded that the bending model of Hobiger et al. (2008) is well applicable for reconstruction of the bending angle above the voxel model, in particular if the voxel model height $h_t$ is set to 12 km or higher.

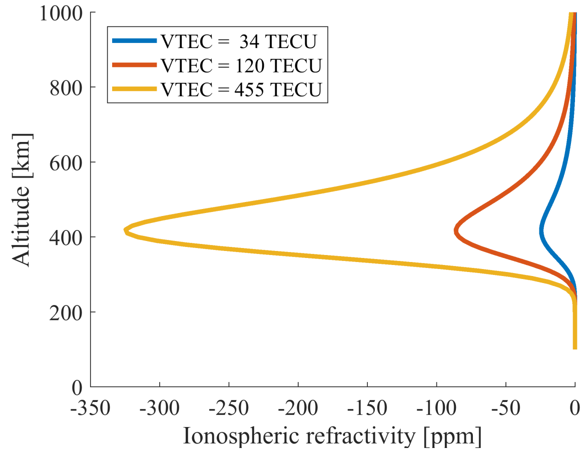


**Figure 5.** Profiles of ionospheric refractivity $N(f)$ assuming signal-frequency $f = 1575.42MHz$

#### 4.2.3 Ionospheric bending effects

Beyond, also the ionosphere influences GNSS signal propagation. In order to assess the impact of free electrons in the ionosphere (above 80 km altitude) on the signal path, the electron density model by Anderson et al. (1987) was executed in three scenarios, assuming a vertical total electron content $(VTEC = \int N_e \cdot dh)$ of 34 TECU (average daytime), 120 TECU (solar maximum) and 455 TECU (maximum possible, see Wijaya, 2010), respectively.

$$N(f) = 10^6 \cdot \frac{-40.2993 \cdot N_e}{f^2} \tag{33}$$

By making use of Eq. (33), the obtained electron density profiles were converted into profiles of refractivity (N), assuming signal frequency $f_1 = 1575.42MHz$ (GPS L1) and $f_2 = 1227.60MHz$ (GPS L2). Figure 5 shows the obtained vertical profiles of ionospheric refractivity, exemplary for frequency $f_1$. The higher the signal-frequency $f$ the lower the phase velocity through the ionosphere and the less is its refraction. Following the approach by Wijaya (2010), the ray paths in the ionosphere were reconstructed, separately for GPS L1 and L2. The analysis revealed significant path differences between the 'true' ray path and its chord line but also between the two signal-frequencies. Assuming a VTEC of 455 TECU and an elevation angle of 3°, the maximum deviation from the straight line signal path is 800 m for L1 and 550 m for L2 respectively, at $h = 400km$, slightly below the layer of peak electron density. Fortunately, ray path deviation decreases significantly with decreasing VTEC and altitude to a few tens of meters at $h = 13.6km$ (the upper rim of the troposphere at which the top of the voxel model was defined). In consequence, the impact of free electrons on the signal path in the lower atmosphere is negligible under moderate and low ionospheric conditions.

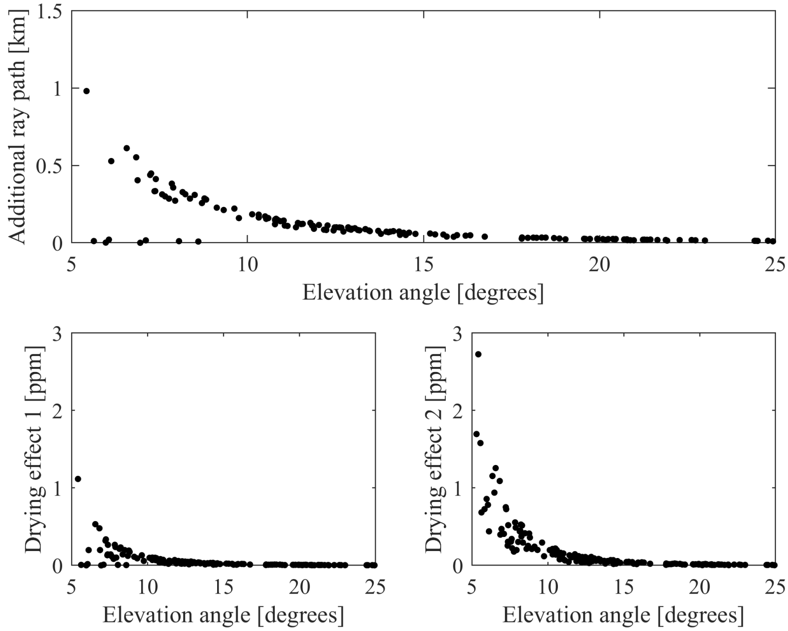


**Figure 6.** Additional ray path caused by straight line assumption (top), the resulting drying effect due to the additional ray path (bottom left) and the resulting drying effect caused by the fact that the straight line ray travels through lower atmospheric levels than the 'true' bended ray (bottom right)

## 5 Impact of atmospheric bending on the tomography solution

In the following, the differences between straight line and bended ray-tracing are further analyzed. For highest consistency, the ray-tracing approach defined in Sect. 4 was used for both, straight line and bended ray-tracing. The only difference is that in case of straight line ray-tracing the ratio $n_i/n_{i+1}$ in Eq. (27) was set to '1'. Thereby, it can be guaranteed that only the impact of atmospheric refraction is assessed.

### 5.1 Expected drying effect

In the beginning, the ray position is equal for both methods but diverges with increasing height. Thereby, the bended ray is travelling in most cases 'above' the straight ray, i.e. the straight ray enters the voxel model top 'earlier' than the bended ray. This leads to the effect that the straight ray remains longer in the voxel model than the bended ray, i.e. the straight ray path within the voxel model $(h < 13.6km)$ is systematically longer than the bended ray path. The differences between both ray paths are plotted in Fig. 6 (top) as function of elevation angle. Therefore, ALARO model data was selected as input for the bended ray-tracer.

The additional ray path decreases rapidly with increasing elevation angle. Thus, a *mixed ray-tracing* approach can be defined, which considers ray bending only for $\varepsilon \leq 15°$. Beyond, the additional ray path is below 0.1 km, and straight line ray-tracing is sufficient for ray path reconstruction.

Figure 6 (top) shows also that in some cases even for low elevation angles the difference in path length is small (below 0.1 km). This appears when the ray enters the voxel model not through the top layer but through a later surface of the voxel model. In this particular case, the difference in path length between both ray-tracing approaches is negligible (be aware that only the entire distance through all voxels is comparable for both ray-tracing approaches but not the individual distances in each voxel). Figure 6 (bottom) shows the expected drying effects in the tomography solution caused by errors in the reconstructed signal paths assuming straight line geometry. Hereby, it is distinguished between the drying effect caused by the additional ray path $(dNw_1)$ and the drying effect caused by the fact that the straight line travels through lower layers of the voxel model $(dNw_2)$. Both effects were assessed as follows:

$$dNw_1 = SWD_b \cdot (d_{k,s} - d_{k,b}) \tag{34}$$

$$dNw_2 = (SWD_b - SWD_s) \cdot d_{k,s} \tag{35}$$

whereby $SWD_b$ and $SWD_s$ are the slant wet delays obtained by ray-tracing through ALARO model data along the bended and the straight line ray path, respectively. The variables $d_{k,b}$ and $d_{k,s}$ are the corresponding path lengths within the voxel model. The sum of their differences along the ray paths are identical with the additional ray paths plotted in Figure 6 (top).

Both drying effects have to be considered as additive and are strongly connected to the current atmospheric conditions as well as to the parametrization applied for interpolation of the refractivity field. In our analysis we assumed an exponential decrease of refractivity between the vertical layers of the voxel model and applied a bi-linear interpolation method for horizontal interpolation between the grid points.

### 5.2 Results from the Austrian GNSS tomography test case

In order to study the impact of bended ray-tracing on the tomography solution, a GNSS tomography test case was defined. The corresponding settings are summarized in Table 1.

Figure 7 (left) shows the differences in wet refractivity between Sol1 and Sol2 (as defined in Table 1). Even though on average over all voxels no bias in wet refractivity is observed, specific voxels show differences in wet refractivity of up to $10ppm$, particularly if due to bending different voxels than in the straight line solution are traversed.

Figure 7 (right) shows the differences in wet refractivity between the first two iterations of the mixed ray-tracing approach (Sol2). In this particular case, refractivity differences are smaller than $0.05ppm$, which implies that the a priori model used for ray-tracing is already close to the 'true' atmospheric conditions, i.e. in this particular case no further iteration was necessary. From all differences in wet refractivity over 248 epochs in May 2013, a maximum of $14.2ppm$, a bias of $0.12ppm$ and a standard deviation of $0.24ppm$ were obtained. Although the bias and standard deviation over all voxels is small, differences of

**Table 1.** Summary of GNSS tomography test case settings

| Parameter | Settings |
|---|---|
| Period | May 2013, 8 epochs per day |
| Voxel domain | Western Austria ($46.4 - 48.0°$ lat, $10.4 - 13.4°$ lon, h = $0 - 13.6km$) |
| Voxel size | $0.4°$ lat x $0.6°$ lon (4 x 5 ground voxels), 15 height layers |
| GNSS data | 30 sec dual-frequency GPS and GLONASS observations - obtained from 6 EPOSA reference sites: SEEF, MATR, JENB, KIBG, ROET, SILL |
| A priori model | ALARO analysis data of temperature and specific humidity - provided on 18 pressure levels in grib1 format for 8 epochs per day |
| Observations | SWDs for all GPS and GLONASS satellites in view above $3°$ elevation angle - derived from 1h ZTD and 2h gradient estimates |
| Ray-tracer | Sol1: Straight line ray-tracing for all observations up to $h = 13.6km$<br>Sol2: Straight line ray-tracing for $\varepsilon > 15°$ and bended ray-tracing for $\varepsilon \leq 15°$ (mixed approach) up to $h = 13.6km$ |

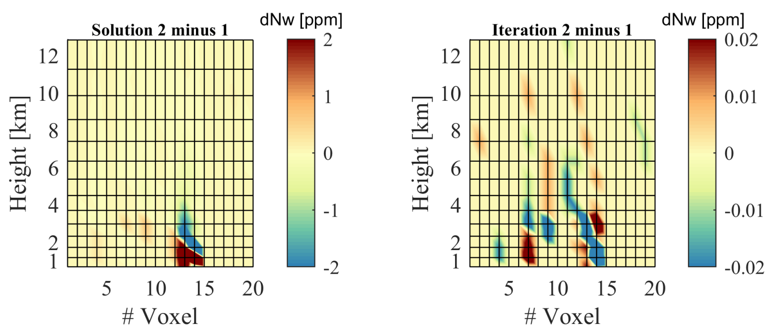


**Figure 7.** Error in wet refractivity caused by straight line assumption (left) and the differences in wet refractivity between first and second iteration (right). Thereby, voxel number '1' is dedicated to the South-West corner and number '20' to the North-East corner of the voxel model. For visualization, a bi-linear interpolation method was applied between the grid points. Analyzed period: May 4, 2013, 15 UTC

about $1ppm$ were observed on average at each epoch, especially when observations below 10 degrees elevation angle enter the tomography solution.

### 5.3 Validation with radiosonde data

For validation of the mixed ray-tracing approach against straight line ray-tracing, the tomography derived wet refractivity fields were compared with radiosonde data at the airport of Innsbruck ($\varphi_i = 47.3°, \lambda = 11.4°, h = 579m$). First, the radiosonde data obtained once a day between 2 and 3 UTC were pre-processed, i.e. outliers in temperature were removed and dew point temperature was converted to water vapor pressure and further to wet refractivity. Finally, the radiosonde profiles were vertically

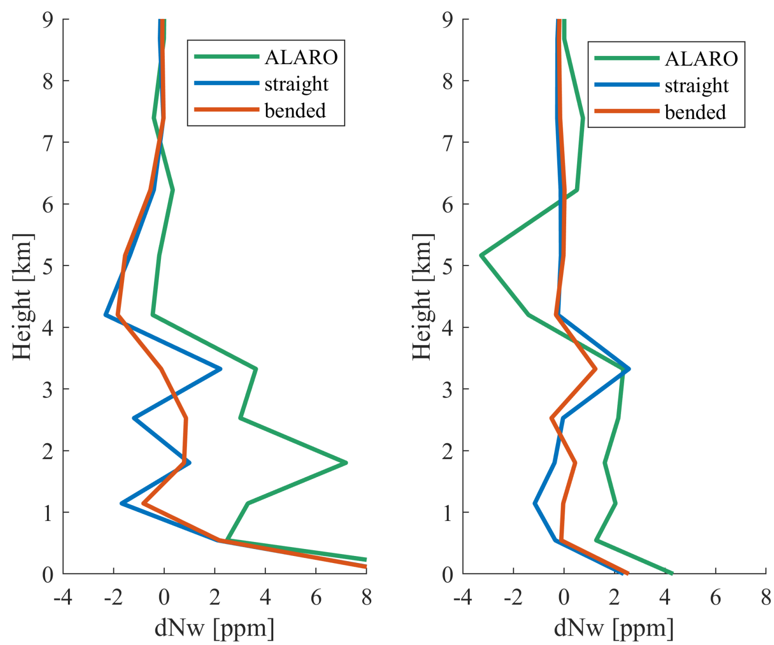


**Figure 8.** Differences in wet refractivity between radiosonde, ALARO and the two tomography solutions based on straight line (blue) and bended ray-tracing (red), exemplary for May 1, 2013, 3 UTC (left) and May 31, 3 UTC (right)

interpolated to the height layers of the voxel model and the tomography derived wet refractivity fields were horizontally interpolated to the ground-position of the radiosonde launching site, respectively. Figure 8 shows the differences in wet refractivity as function of height above surface, exemplarily for two epochs in May, 2013. In both cases, the bended ray-tracing approach helps to reduce the tomography error by about $1-2ppm$, especially in the lower 4 km of the atmosphere. Largest differences are visible when the bended ray traverses other voxels than its chord line. This appeared in about 2 % of the test cases, especially if observations below 10 degrees elevation angle enter the tomography solution.

## 6 Conclusions

GNSS signals which enter the neutral atmosphere at low elevation angles ($\varepsilon$ < 15 degrees) are significantly affected by atmospheric bending. In case the bending is neglected when setting up design matrix $\boldsymbol{A}$, a systematic error of up to $10-20ppm$, on average of $1-2ppm$ is introduced into the GNSS tomography solution. This error can be widely reduced if atmospheric bending is considered in reconstruction of the signal paths. Therefore, a 2D piecewise linear ray-tracing approach was defined, which describes the bended GNSS signal path by small line segments. By limiting the length of the line segments to $100m$ in case of $\varepsilon = 3°$ or even shorter for higher elevation angles, the 'true' signal path can be widely reconstructed. However, the quality of the reconstructed signal paths depends primarily on the quality of the a priori refractivity field. Comparisons between refractivity fields derived from standard atmosphere and ALARO weather model data reveal that a refractivity error of $30ppm$ can cause a ray deviation of up to several hundred meters, i.e. the distance traveled in each voxel but also the number of traversed voxels is prone to misallocations. In consequence, reliable a priori data, e.g. derived from numerical weather model data, are recommended for GNSS tomography.

Nevertheless, if reliable a priori data are not available or if the quality is unknown, iterative ray-tracing helps for reducing the impact of wet refractivity errors on the tomography solution. Therefore, the wet refractivity field obtained from an initial tomography solution is used for reconstruction of the signal paths for the next iteration. The processing is repeated until the tomography solution converges. This ensues usually after two iterations. Beyond, a bending model, like the one provided by Hobiger et al. (2008) helps to significantly reduce computational cost by describing the remaining bending in the higher atmosphere (above the voxel model). In consequence, the ray-tracer can be stopped right after the reconstructed signal leaves the voxel model. In case of $h_t = 13.6km$, the number of processing steps is reduced by $85\%$, which is a tremendous reduction in processing time without significant loss of accuracy.

In contrast, ionospheric bending effects have less impact on the GNSS tomography solution. Even during periods of solar maximum, ray path deviation caused by ionospheric bending is negligible for signals in L-band $(1-2GHz)$. However, even if ionospheric bending has no impact on the tomography solution, first and higher order ionospheric effects should be taken into account when processing GNSS phase observations.

Besides, comparisons with radiosonde data revealed that if atmospheric bending effects are considered in GNSS tomography, the quality of the tomography solution can be improved by $1-2ppm$. Within the defined test case, especially voxels in the lower $4km$ of the atmosphere benefitted from the applied mixed ray-tracing approach. Due to significant optimization, the mixed ray-tracing approach ensures processing of large tomography test cases in adequate time. A test case with 72 GNSS sites and 7 x 9 x 15 voxels can be processed in less than two minutes. Thus, the developed mixed ray-tracing approach is applicable also in near real-time and therefore well suited for operational purposes.

*Code availability.* The 2D piecewise linear ray-tracer for GNSS tomography as well as the RADIATE ray-tracer are part of the Vienna VLBI and Satellite Software (VieVS). The code of the RADIATE ray-tracer is available at https://github.com/TUW-VieVS/RADIATE. For more details to VieVS, the reader is referred to http://vievswiki.geo.tuwien.ac.at.

## Appendix A: Unmodelled bending effects in the Vienna hydrostatic mapping function

In case of VMF1 (Böhm et al., 2006) or similar mapping concepts, azimuthal asymmetry is not considered and for convenience, only a single hydrostatic mapping coefficient per site $(a_h)$ is determined as follows:

$$a_h = -\frac{mf_h(\varepsilon)\cdot\sin\varepsilon - 1}{\frac{mf_h(\varepsilon)}{\sin\varepsilon + \frac{b_h}{\sin\varepsilon + c_h}} - \frac{1}{1+\frac{b_h}{1+c_h}}}. \tag{A1}$$

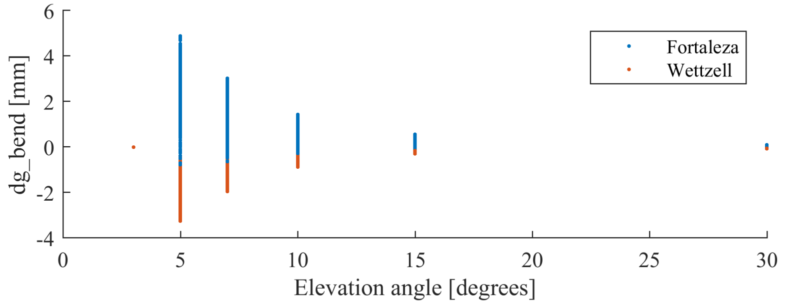


**Figure A1.** The unmodeled geometric bending effect in VMF1 hydrostatic mapping function ($dg_{bend}$), exemplary for VLBI sites Fortaleza, Brazil and Wettzell, Germany. Analyzed period: Jan-Feb 2014

where $b_h$ is 0.0029, $c_h$ depends on the day of year and latitude and $mf_h(\varepsilon)$ is defined as the ratio between $SHD(3°)$ and $ZHD$, obtained by ray-tracing through numerical weather model data. For assessing the remaining unmodeled geometric bending $dg_{bend}(\varepsilon,\alpha)$, ray-traced slant hydrostatic delays were compared with 'mapped' slant hydrostatic delays as follows:

$$dg_{bend}(\varepsilon,\alpha)[m] = ZHD[m] \cdot mf_h(\varepsilon) - ZHD[m] \cdot mf_{h0}(\varepsilon) - g_{bend}(\varepsilon,\alpha)[m] \tag{A2}$$

where $ZHD$ is the zenith hydrostatic delay obtained by vertical integration, $g_{bend}(\varepsilon,\alpha)$ is the geometric bending effect as obtained by ray-tracing, $mf_h(\varepsilon)$ is the VMF1 hydrostatic mapping function determined by $SHD(3°)/ZHD$ and $mf_{h0}(\varepsilon)$ is the hydrostatic mapping function determined by $SHD_0(3°)/ZHD$, whereby $SHD(3°)$ and $SHD_0(3°)$ are the slant hydrostatic delays obtained by ray-tracing for an vacuum elevation angle $\varepsilon_k = 3°$ with and without geometric bending, respectively. Figure A1 shows the remaining unmodeled geometric bending as obtained for six elevation angles (and 16 equidistant azimuth angles), exemplary for the two VLBI sites Fortaleza, Brazil ($\varphi = -3.9°, \lambda = 321.6°, h = 23m$) and Wettzell, Germany ($\varphi = 49.1°, \lambda = 12.9°, h = 669m$). In case of $\varepsilon = 3°$, almost no bending error is visible since $mf_h(\varepsilon)$ was tuned for this elevation angle. However, for other elevation angles, the unmodeled geometric bending is about 3 % of the slant hydrostatic delay, e.g. up to $\pm 5mm$ at $5°$ elevation angle. In case of Wettzell, $dg_{bend}(\varepsilon,\alpha)$ is mostly negative, i.e. the 'mapped' $SHD$ is smaller than the observed $SHD$ and vice versa for Fortaleza. So far, these small variations are neglected when using VMF1 hydrostatic mapping function in GNSS signal processing.

*Acknowledgements.* Open access funding was provided by Austrian Science Fund (FWF). The authors would like to thank the Austrian Science Fund (FWF) for financial support of this study within the project RADIATE ORD (ORD 86) and the Austrian Research Promotion Agency (FFG) for finacial support within the project GNSS-ATom (840098).

## References


Aghajany, S. H. and Amerian, Y.: Three dimensional ray tracing technique for tropospheric water vapor tomography using GPS measurements, J. Atmospheric Sol.-Terr. Phys., 164, 81–88, https://doi.org/10.1016/j.jastp.2017.08.003, 2017.

Anderson, D. N., Mendillo, M., and Herniter, B.: A semi-empirical low-latitude ionospheric model, Radio Sci., 22, 292–306, https://doi.org/10.1029/RS022i002p00292, 1987.

Bender, M. and Raabe, A.: Preconditions to ground based GPS water vapour tomography, Ann. Geophys., 25, 1727–1734, https://doi.org/10.5194/angeo-25-1727-2007, 2007.

Bender, M., Stosius, R., Zus, F., Dick, G., Wickert, J., and Raabe, A.: GNSS water vapour tomography - Expected improvements by combining GPS, GLONASS and Galileo observations, Adv. Space Res., 47, 886–897, https://doi.org/10.1016/j.asr.2010.09.011, 2011.

Bevis, M., Businger, S., Herring, T. A., Rocken, C., Anthes, R. A., and Ware, R. H.: GPS meteorology: Remote sensing of atmospheric water vapor using the Global Positioning System, J. Geophys. Res., 97, 15 787–15 801, https://doi.org/10.1029/92JD01517, 1992.

Böhm, J., Werl, B., and Schuh, H.: Troposphere mapping functions for GPS and Very Long Baseline Interferometry from European Centre for Medium-Range Weather Forecasts operational analysis data, J. Geophys. Res., 111, 1–9, https://doi.org/10.1029/2005JB003629, 2006.

Champollion, C., Masson, F., Bouin, M.-N., Walpersdorf, A., Doerflinger, E., Bock, O., and Bealen, J. V.: GPS water vapour tomography: preliminary results from the ESCOMPTE field experiment, Atm. Res., 74, 253–274, https://doi.org/10.1016/j.atmosres.2004.04.003, 2005.

Chen, G. and Herring, T. A.: Effects of atmospheric azimuthal asymmetry on the analysis of space geodetic data, J. Geophys. Res., 102, 20 489–20 502, https://doi.org/10.1029/97JB01739, 1997.

Flores Jimenez, A.: Atmospheric tomography using satellite radio signals, Ph.D. thesis, Universitat Politecnica de Catalunya, Departament de Teoria del Senyal i Comunicacions, http://www.tdx.cat/handle/10803/6881, 1999.

Hansen, P. C.: The L-curve and its use in the numerical treatment of inverse problems, in: Computational Inverse Problems in Electrocardiology, Advances in Computational Bioengineering, ISBN: 1853126144, pp. 119–142, WIT Press, 2000.

Hirahara, K.: Local GPS tropospheric tomography, Earth Planets Space, 52, 935–939, https://doi.org/10.1186/BF03352308, 2000.

Hobiger, T., Ichikawa, R., Koyama, Y., and Kondo, T.: Fast and accurate ray-tracing algorithms for real-time space geodetic applications using numerical weather models, J. Geophys. Res., 113, 1–14, https://doi.org/10.1029/2008JD010503, 2008.

Hofmeister, A.: Determination of path delays in the atmosphere for geodetic VLBI by means of ray-tracing, Ph.D. thesis, TU Wien, Department of Geodesy and Geoinformation, http://repositum.tuwien.ac.at/obvutwhs/content/titleinfo/1370367, 2016.

Iyer, H. M. and Hirahara, K.: Seismic tomography: Theory and practice, Springer Netherlands, iSBN: 0412371901, 1993.

Kruse, L. P.: Spatial and Temporal Distribution of Atmospheric Water Vapor using Space Geodetic Techniques, Geodätisch-geophysikalische Arbeiten in der Schweiz, 61, 2001.

Landskron, D. and Böhm, J.: Refined discrete and empirical horizontal gradients in VLBI analysis, J. Geod., 92, 1387–1399, https://doi.org/10.1007/s00190-018-1127-1, 2018.

MacMillan, D. S.: Atmospheric gradients from Very Long Baseline Interferometry observations, Geophys. Res. Lett., 22, 1041–1044, https://doi.org/10.1029/95GL00887, 1995.

Manning, T.: Sensing the dynamics of severe weather using 4D GPS tomography in the Australien region, Ph.D. thesis, Royal Melbourne Institute of Technology, School of Mathematical and Geospatial Sciences, http://researchbank.rmit.edu.au/eserv/rmit:160752/Manning.pdf, 2013.

Möller, G.: Reconstruction of 3D wet refractivity fields in the lower atmosphere along bended GNSS signal paths, Ph.D. thesis, TU Wien, Department of Geodesy and Geoinformation, http://repositum.tuwien.ac.at/obvutwhs/content/titleinfo/2268559, 2017.

Nievinski, F. G.: Ray-tracing to mitigate the neutral atmosphere delay in GPS, Master's thesis, University of New Brunswick, Department of Geodesy and Geomatics Engineering, http://www2.unb.ca/gge/Pubs/TR262.pdf, 2009.

Nilsson, T.: Assessment of tomographic methods for estimation of atmospheric water vapor using ground-based GPS, Ph.D. thesis, Chalmers University of Technology, Göteborg, Department of Radio and Space Science, Sweden, 2005.

Raymond, T. D., Franke, S. J., and Yeh, K. C.: Ionospheric tomography: its limitations and reconstruction methods, J. Atmospheric Terr. Phys., 56, 637–657, https://doi.org/10.1016/0021-9169(94)90104-X, 1994.

Steiner, A. K., Löscher, A., and Kirchengast, G.: Error characteristics of Refractivity Profiles Retrieved from CHAMP Radio Occultation Data, pp. 27–36, Springer Berlin Heidelberg, Atmosphere and Climate: Studies by Occultation Methods, https://doi.org/10.1007/3-540-34121-8_3, 2006.

Wijaya, D. D.: Atmospheric correction formulae for space geodetic techniques, Ph.D. thesis, Graz University of Technology, Faculty of Technical Mathematics and Technical Physics, http://www.shaker.de/Online-Gesamtkatalog-Download/2018.11.26-19.55.57-207.151.220.142-rad6E460.tmp/3-8322-8994-1_INH.PDF, 2010.

Zou, X., Vandenberghe, F., Wang, B., Gorbunov, M. E., Kuo, Y., Sokolovskiy, S., Chang, J. C., Sela, J. G., and Anthes, R. A.: A ray-tracing operator and its adjoint for the use of GPS/MET refraction angle measurements, J. Geophys. Res.: Atmospheres, 104, 22 301–22 318, https://doi.org/10.1029/1999JD900450, 1999.

Zus, F., Dick, G., Heise, S., and Wickert, J.: A forward operator and its adjoint for GPS slant total delays, Radio Sci., 50, 393–405, https://doi.org/10.1002/2014RS005584, 2015.

# Atmospheric bending effects in GNSS tomography

Gregor Möller[1] and Daniel Landskron[1]

[1]Department of Geodesy and Geoinformation, Vienna University of Technology, Vienna, Austria

**Correspondence:** Gregor Möller (gregor.moeller@tuwien.ac.at)

**Abstract.** In GNSS tomography, precise information about the tropospheric water vapor distribution is derived from integral measurements like ground-based GNSS slant wet delays (SWDs). Therefore, the functional relation between observations and unknowns, i.e. the signal paths through the atmosphere have to be accurately known for each station-satellite pair involved. ~~Since GNSS signals~~ For GNSS signals observed above 15 degrees elevation angle, the signal path is well approximated by a straight line. However, since electromagnetic waves are prone to atmospheric bending effects, ~~a straight line~~ this assumption is not sufficient ~~for elevation angles $< 15°$~~anymore for lower elevation angles. Thus, in the following, a mixed 2D piecewise linear ray-tracing approach is introduced and possible error sources in reconstruction of the bended signal paths are analyzed in more detail. Especially, if low elevation observations ~~($\varepsilon < 10°$)~~ are considered, unmodeled bending effects can introduce a systematic error of up to ~~$10-20ppm$~~$10-20ppm$, on average of ~~$1-2ppm$~~ $1-2ppm$ into the tomography solution. Thereby, not only the ray-tracing ~~approach itself but primarily~~ method but also the quality of the a priori field ~~has~~ can have a significant impact on the ~~reconstruction quality~~reconstructed signal paths, if not reduced by iterative processing. In order to ~~overcome possible limitations in the a priori field, an iterative tomography processing strategy is applied. Further~~keep the processing time within acceptable limits, a bending model is applied for the upper part of the neutral atmosphere. It helps to reduce the number of processing steps by up to 85% ~~. In consequence~~without significant degradation in accuracy. Therewith, the developed mixed ray-tracing approach allows not only for a correct treatment of low elevation observations but is also fast and applicable for near real-time applications.

## 1 Introduction

For conversion of precise integral measurements into two- or three-dimensional structures, a technique called tomography has been invented. In the field of GNSS meteorology, the principle of tomography became applicable with the increasing number of ~~GNSS~~ Global Navigation Satellite System (GNSS) satellites and the build-up of densified ground-based GNSS networks in the 1990s (Raymond et al., 1994; Flores Jimenez, 1999). ~~According to Iyer and Hirahara (1993), the general principle of tomography is described as follows:~~

$$\cancel{f_s = \int_S g_s \cdot ds}$$

~~where $f_s$ is the projection function, $g_s$ is the object property function and $ds$ is a small element of the ray path S along which the integration takes place. In GNSS meteorology, $g_s$ is usually replaced by refractive index $n-1$, and integral measure $f_s$ by~~

~~the GNSS signal delay in the neutral atmosphere ($STD$)~~

$$STD = \int_R n \cdot ds - \int_S ds$$

~~where R is the true signal path and S is the theoretical straight-line signal path in vacuum. A full non-linear solution for the refractive index $n$ is not of practical relevance since according to Fermat´s principle, first order changes of the ray path lead to second order changes in travel time. In consequence, by ignoring the path dependency in the inversion of $n$ along $ds$ and by assuming the ray path as a straight line, a linear tomography approach can be defined which is well applicable to $STDs$ above $15°$ elevation angle (Möller, 2017). However, with decreasing elevation angle, the true signal path deviates significantly from a straight line. In consequence, by ignoring atmospheric bending, a systematic error is introduced in the tomography solution. In order to overcome this limitation, in the following an *iterative tomography approach* is defined in which the bended signal path is approximated by small line segments. Similar to the linear tomography approach, thereby the neutral atmosphere or parts of it are discretized in volume elements (voxels) in which the refractivity $N_k = (n_k - 1) \cdot 10^6$ in each voxel $k$ is assumed as constant. Consequently, Eq. (2) can be replaced by :~~

$$STD = \sum_{k=1}^{m} N_K \cdot d_k$$

~~where $d_k$ is the travelled distance in each voxel. Assuming $l$ observations and $m$ voxels, a linear equation system can be set up. In matrix notation it reads:~~

$$\boldsymbol{STD} = \boldsymbol{A} \cdot \boldsymbol{N}$$

~~where $\boldsymbol{STD}$ is the observation vector of size $(l,1)$, $\boldsymbol{N}$ is the vector of unknowns of size $(m,1)$ and $\boldsymbol{A}$ is a matrix of size $(l,m)$ which contains the partial derivatives of the slant total delays with respect to the unknowns, i.e. the travelled distances $d_k$ in each voxel.~~

$$\boldsymbol{A} = \begin{bmatrix} \frac{\delta STD_1}{\delta N_1} & \cdots & \frac{\delta STD_1}{\delta N_m} \\ \vdots & \ddots & \vdots \\ \frac{\delta STD_l}{\delta N_1} & \cdots & \frac{\delta STD_l}{\delta N_m} \end{bmatrix}$$

~~In case of slant wet delays ($SWDs$), Eq. (4) can be rewritten as follows:~~

$$\boldsymbol{SWD} = \boldsymbol{A} \cdot \boldsymbol{N_w}$$

~~where $\boldsymbol{N_w}$ contains the wet refractivities in each voxel. In case a priori information ($\boldsymbol{N_{w0}}$) can be made available, it enters the least squares tomography solution as follows:~~

$$\boldsymbol{N_w} = \boldsymbol{N_{w0}} + \boldsymbol{V} \cdot \boldsymbol{S}^{-1} \cdot \boldsymbol{U}^T \cdot \boldsymbol{A}^T \cdot \boldsymbol{P} \cdot (\boldsymbol{SWD} - \boldsymbol{A} \cdot \boldsymbol{N_{w0}})$$

~~where matrix $\boldsymbol{U}$, $\boldsymbol{V}$ and $\boldsymbol{S}$ are obtained by singular value decomposition of matrix $\boldsymbol{A}^T \cdot \boldsymbol{P} \cdot \boldsymbol{A} + \boldsymbol{P_c}$. For further details, the reader is referred to Möller (2017). In order to determine $\boldsymbol{N_w}$, weighting matrices $\boldsymbol{P}$ and but also the travelled distances $d_k$ in each voxel have to be determined.~~ Since then, a variety of tomography approaches based on raw GNSS phase measurements (Nilsson, 2005), double difference residuals (Kruse, 2001), slant delays (Flores Jimenez, 1999; Hirahara, 2000) or slant integrated water vapor (Champollion et al., 2005) has been developed for the accurate reconstruction of the water vapor distribution in the lower atmosphere. An overview about the major developments within this field of research since Flores Jimenez (1999) is provided by Manning (2013).

While in most tomography approaches, observations gathered at low elevation angles are discarded (Bender et al., 2011; Champollion et al., 2005; Hirahara, 2000), ~~straight-line~~ straight line signal path reconstruction is sufficient for the determination of the ~~paths~~ path lengths. However, ~~a correct tomographysolution based on~~ Bender and Raabe (2007) showed that especially low elevation observations can be a very useful source of information in GNSS tomography. Besides their information content about the lower troposphere, the additional observations strengthen the observation geometry and therewith, contribute to a more reliable tomography solution. However, a correct treatment of low elevation observations ~~is longing for~~ requires more advanced ray-tracing algorithms. The first paper which deals with bended ray path reconstruction in GNSS tomography was published by ~~Aghajany and Amerian (2017), who compared different~~ Zus et al. (2015), with main focus on the reconstruction of the signal paths for delay estimation but also for assimilation of GNSS slant delays into numerical weather prediction systems. Most recently, Aghajany and Amerian (2017) published their results about 3D ray-tracing ~~approaches~~ in water vapor tomography and briefly analyzed its impact on the tomography solution.

~~In the~~ Based on the existing studies, in the following, a more detailed discussion of possible error sources in signal path reconstruction is provided. Therefore, Sect. 2 describes the effect of atmospheric bending and its handling in GNSS signal processing. Section 3 ~~deals with the~~ describes the principles of GNSS tomography and how the basic equation of tomography is solved for wet refractivity. Section 4 introduces the concept for reconstruction of signal paths using ray-tracing techniques. Hereby, the modified piecewise linear ray-tracing approach is ~~introduced~~ described - including its ability for reconstruction of the GNSS signal geometry. In Sect. ~~4~~5, the defined ray-tracing approach is applied to real SWDs and its impact on the tomography solution is assessed and validated against radiosonde data. Section ~~5~~ 6 concludes the major findings.

## 2 Atmospheric bending effects in GNSS signal processing

The effect of atmospheric bending on GNSS signals is related to the propagation properties of electromagnetic waves. In vacuum, GNSS signals travel with the velocity of light. When entering into the atmosphere, the electromagnetic wave velocity changes, dependent on the electric permittivity ($\epsilon$) and magnetic permeability ($\mu$) of the atmospheric constituents and the frequency of the electromagnetic wave. The ratio between the velocity of light $c$ in vacuum and the velocity $\nu$ in a medium defines the refractive index $n$.

$$n = \frac{c}{\nu} = \sqrt{\frac{\epsilon \cdot \mu}{\epsilon_0 \cdot \mu_0}} \tag{1}$$

For signals in the microwave frequency-band, $n$ ranges ~~usually~~ from 0.9996 to 1.0004~~, which goes along with a wave velocity slightly higher or lower than the velocity of light.~~

$$n_i \cdot \sin\Theta_i = n_0 \cdot \sin\Theta_0$$

~~In consequence and according to Eq. (9), the electromagnetic wave experiences thereby a curvature effect (change in angle of incidence $\Theta$ for $\Theta_0 \neq 0$), also known as atmospheric bending. In GNSS signal processing both effects, the change in velocity but also the deviation of the signal path from a straight line, have to be taken into account since both cause a change in atmospheric signal travel time ($\Delta\rho$)~~. Thus, $n$ is usually replaced by refractivity $N$, expressed in mm/km (ppm).

$$N = 10^6 \cdot (n-1) \tag{2}$$

The GNSS signal delay in the lower atmosphere, also known as slant total delay ($STD$), is related to refractivity by the following equation (Bevis et al., 1992):

$$\Delta\rho STD = \frac{1}{c} 10^{-6} \cdot \int\limits_R nN \cdot ds - \int\limits_R ds + \frac{1}{c} \cdot \left[\int\limits_R ds - \int\limits_S ds\right] \tag{3}$$

The first term of Eq. (~~10~~3) describes the change in travel time due to velocity changes along the true ray path R. The second term (about three orders of magnitude smaller than the first term) is related to the difference in geometrical path length between the true (R) and the chord signal path (S). ~~However, in most GNSS applications not the true signal path but rather its impact on the signal travel time is modelled – separately for neutral troposphere (Bevis et al., 1992) and ionosphere (Fritsche et al., 2005). For highest precision, the GNSS signal delay in the neutral atmosphere or parts of it on top of an a priori model are estimated together with other parameters of interest using~~ According to Dalton's law, the refractivity of air can be split up into a hydrostatic and a wet component: $N = N_h + N_w$. Therewith, the GNSS signal delay reads:

$$STD = SHD + SWD = 10^{-6} \cdot \int\limits_R N_h \cdot ds + 10^{-6} \cdot \int\limits_R N_w \cdot ds + \left[\int\limits_R ds - \int\limits_S ds\right]. \tag{4}$$

The slant wet delay ($SWD$) depends on the wet refractivity along the true ray path $R$.

$$SWD = 10^{-6} \cdot \int\limits_R N_w \cdot ds \tag{5}$$

The slant hydrostatic delay ($SHD$) results from the the hydrostatic refractivity along $R$ and, by definition, from the additional path length due to atmospheric bending.

$$SHD = 10^{-6} \cdot \int\limits_R N_h \cdot ds + \left[\int\limits_R ds - \int\limits_S ds\right] \tag{6}$$

While signal path $S$ follows from the straight line geometry between satellite and receiver, the true signal path $R$ depends in addition on the hydrostatic and the wet refractivity distribution along the signal path (see Sect. 3 for more details).

In GNSS signal processing, the integral along the signal path is usually replaced by the zenith delay and a mapping function. Therefore, Eq. (~~11) . Therefore, the $STD$ is split into three components, namely hydrostatic, wet and asymmetric delay:~~ 4) is rewritten as follows:

$$STD(\varepsilon,\alpha) = SHD + SWD = ZHD \cdot mf_h(\varepsilon) + ZWD \cdot mf_w(\varepsilon) + G(\varepsilon,\alpha) \quad (7)$$

where $ZHD$ is the zenith hydrostatic delay, $ZWD$ is the zenith wet delay and $mf_h$ and $mf_w$ are the corresponding mapping functions, which describe the elevation ($\varepsilon$) dependency of the signal delay. The elevation and azimuth ($\alpha$) dependent first-order horizontally asymmetric term $G(\varepsilon,\alpha)$ reflects local variations in the atmospheric conditions~~;~~: see MacMillan (1995), Chen and Herring (1997) or Landskron and Böhm (2018). In practice, e.g. when using VMF1 mapping function (Böhm et al., 2006) or similar mapping concepts, the tropospheric delay due to atmospheric bending is absorbed by the hydrostatic mapping function term $mf_h$. Comparisons between ray-traced $SHD(\varepsilon)$ and 'mapped' $SHD(\varepsilon) = ZHD \cdot mf_h(\varepsilon)$ slant hydrostatic delays reveal that about 97 % of the atmospheric bending effect is compensated by the VMF1 hydrostatic mapping function (see Appx. A for further details).

## 3 The principles of GNSS tomography

According to Iyer and Hirahara (1993), the general principle of tomography is described as follows:

$$f_s = \int_R g_s \cdot ds \quad (8)$$

where $f_s$ is the projection function, $g_s$ is the object property function and $ds$ is a small element of the ray path $R$ along which the integration takes place. In GNSS tomography, $g_s$ is usually replaced by wet refractivity $N_w$, and integral measure $f_s$ by $SWD$ (the prefactor of $10^6$ vanishes if $ds$ is provided in kilometer and $SWD$ in millimeter).

$$SWD = \int_R N_w \cdot ds \quad (9)$$

A full non-linear solution of Eq. (9) for wet refractivity is not of practical relevance since according to Fermat´s principle, first order changes of the ray path lead to second order changes in travel time. In consequence, by ignoring the path dependency in the inversion of $N_w$ along $ds$ and by assuming the ray path as a straight line, a linear tomography approach can be defined which is well applicable to $SWDs$ above 15 degrees elevation angle (Möller, 2017). However, with decreasing elevation angle, the true signal path deviates significantly from a straight line. In consequence, by ignoring atmospheric bending, a systematic error is introduced in the tomography solution. In order to overcome this limitation, in the following an *iterative tomography approach* is defined in which the bended signal path is approximated by small line segments. Similar to the linear tomography approach, thereby the neutral atmosphere or parts of it are discretized in volume elements (voxels) in which the refractivity

$N_{w,k}$ in each voxel $k$ is assumed as constant. Consequently, Eq. (9) can be replaced by:

$$SWD = \sum_{k=1}^{m} N_{w,k} \cdot d_k \tag{10}$$

where $d_k$ is the travelled distance in each voxel. Assuming $l$ observations and $m$ voxels, a linear equation system can be set up. In matrix notation it reads:

$$\boldsymbol{SWD} = \boldsymbol{A} \cdot \boldsymbol{N_w} \tag{11}$$

where $\boldsymbol{SWD}$ is the observation vector of size $(l,1)$, $\boldsymbol{N_w}$ is the vector of unknowns of size $(m,1)$ and $\boldsymbol{A}$ is a matrix of size $(l,m)$ which contains the partial derivatives of the slant wet delays with respect to the unknowns, i.e. the travelled distances $d_k$ in each voxel.

$$\boldsymbol{A} = \begin{bmatrix} \frac{\delta SWD_1}{\delta N_{w,1}} & \cdots & \frac{\delta SWD_1}{\delta N_{w,m}} \\ \vdots & \ddots & \vdots \\ \frac{\delta SWD_l}{\delta N_{w,1}} & \cdots & \frac{\delta SWD_l}{\delta N_{w,m}} \end{bmatrix} \tag{12}$$

Solving Eq. (11) for $\boldsymbol{N_w}$ requires the inversion of matrix $\boldsymbol{A}$.

$$\boldsymbol{N_w} = \boldsymbol{A^{-1}} \cdot \boldsymbol{SWD} \tag{13}$$

The inverse $\boldsymbol{A^{-1}}$ exists if $\boldsymbol{A}$ is squared and if the determinant of $\boldsymbol{A}$ is non-zero, otherwise matrix $\boldsymbol{A}$ is called singular. Unfortunately, singularity appears in GNSS tomography in most cases since the observation data is 'incomplete' and matrix $\boldsymbol{A}$ is not of full rank. Therewith, Eq. (13) becomes ill-posed, i.e. not uniquely solvable. In order to find a solution which preserves most properties of an inverse, in the following matrix $\boldsymbol{A}$ is replaced by pseudo inverse $\boldsymbol{A^+}$. According to Hansen (2000) the pseudo inverse is defined as follows:

$$\boldsymbol{A^+} = \boldsymbol{V} \cdot \boldsymbol{S^{-1}} \cdot \boldsymbol{U^T} \tag{14}$$

where U and V are orthogonal, normalized left and right singular vectors of A and matrix S is a diagonal matrix, which contains the singular values in descending order. In case a priori information ($\boldsymbol{N_{w0}}$) can be made available, it enters the tomography solution as first guess as follows:

$$\boldsymbol{N_w} = \boldsymbol{N_{w0}} + \boldsymbol{V} \cdot \boldsymbol{S}^{-1} \cdot \boldsymbol{U}^T \cdot \boldsymbol{A}^T \cdot \boldsymbol{P} \cdot (\boldsymbol{SWD} - \boldsymbol{A} \cdot \boldsymbol{N_{w0}}) \tag{15}$$

where matrix $\boldsymbol{U}$, $\boldsymbol{V}$ and $\boldsymbol{S}$ are obtained by singular value decomposition of matrix $\boldsymbol{A}^T \cdot \boldsymbol{P} \cdot \boldsymbol{A} + \boldsymbol{P_c}$. The weighting matrices $\boldsymbol{P}$ and $\boldsymbol{P_c}$ are defined as the inverse of the variance-covariance matrix $\boldsymbol{C}$ for the observations and $\boldsymbol{C_c}$ for the first guess, respectively. Assuming, that the observations are uncorrelated, the non-diagonal elements of $\boldsymbol{C}$ and $\boldsymbol{C_c}$ are zero and the diagonal elements are defined as follows:

$$\sigma_C^2 = \sin^2 \varepsilon \cdot \sigma_{ZWD}^2 \tag{16}$$

$$\sigma_{C_c}^2 = \left(\frac{\partial N_w}{\partial T} \cdot \sigma_T\right)^2 + \left(\frac{\partial N_w}{\partial q} \cdot \sigma_q\right)^2 + \left(\frac{\partial N_w}{\partial p} \cdot \sigma_p\right)^2 \tag{17}$$

whereby $\sigma_{ZWD} = 2.5mm$ reflects the uncertainty of the $ZWD$. The values for $\sigma_T$, $\sigma_q$ and $\sigma_p$ were taken from height-dependent error curves for pressure $(p)$, temperature $(T)$ and specific humidity $(q)$ as provided by Steiner et al. (2006) for the ECMWF (European Centre for Medium-Range Weather Forecasts) analysis data. For further details, the reader is referred to Möller (2017) .

## 4 Reconstruction of GNSS signal paths

Assuming that the geometrical optics approximation is valid and that the atmospheric conditions change only inappreciably within one wavelength, the signal path is well reconstructible by means of ray-tracing shooting techniques (Hofmeister, 2016; Nievinski, 2009). Thereby, the basic equation for ray-tracing, the so-called Eikonal equation, has to be solved for obtaining optical path length $L$.

$$||\nabla L||^2 = n(\boldsymbol{r})^2 \tag{18}$$

From Eq. (~~12~~18), a number of 3D and 2D ray-tracing approaches have been derived ~~(Hobiger et al., 2008).~~ for the reconstruction of ground-based and space-based GNSS measurements and of their signal paths through the atmosphere (Hobiger et al., 2008; Zou et al., 19 .

The main difference between both observation types is related to the observation geometry. While for space-based GNSS observations derived in limb sounding, the bending angle is usually described as function of impact parameter $a$, for ground-based observations elevation and azimuth angle are used for characterizing the signal geometry. In consequence, the optimal ray-tracing approach will be significantly different for various observation geometries.

In order to find ~~the~~ an optimal approach for operational analysis of ground-based measurements, Hofmeister (2016) carried out a number of exploratory comparisons. Based on the outcome, the 2D piecewise linear ray-tracer was defined as the optimal reconstruction tool for the iterative reconstruction of the atmospheric signal delays including atmospheric bending. It is limited to positive elevation angles but it is fast and almost as accurate as the 3D ray-tracer~~, however for application~~ . However, for the use in GNSS tomography, the ray-tracing approach had to be further modified. In the following, the developed ~~mixed~~ ray-tracing approach but also its impact on the GNSS tomography solution are discussed in more detail.

### 4.1 Piecewise linear ray-tracer

The starting point for the 2D piecewise linear ray-tracer is the receiver position in ellipsoidal coordinates $(\varphi_1, \lambda_1, h_1)$, the '~~outgoing~~vacuum' elevation angle $\varepsilon_k$ (see Fig. 1) and the azimuth angle $\alpha$ under which the satellite is observed. In case of GNSS ~~signals, both angles~~ tomography, these parameters can be determined with sufficient accuracy from satellite ephemerides

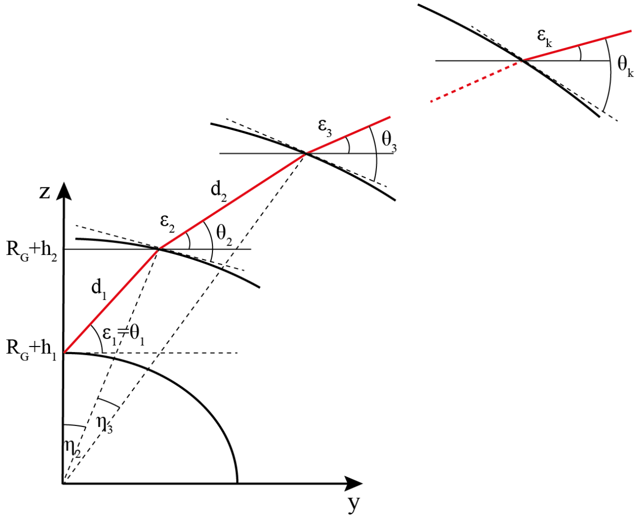


**Figure 1.** Geometry of the ray-tracing approach with the geocentric coordinates (y, z), the geocentric angles $(\eta, \theta)$, elevation angle $\varepsilon$ and $d$ as the distance between two consecutive ray points

and the receiver position - assuming straight line geometry. ~~In consequence~~Therewith, the initial parameters for ray-tracing (see Fig. 1), i.e. the geocentric coordinates $(y_1, z_1)$ and the corresponding geocentric angles $(\eta_1, \theta_1)$ read:

$$y_1 = 0 \tag{19}$$

$$z_1 = R_G + h_1 \tag{20}$$

$$\eta_1 = 0 \tag{21}$$

$$\theta_1 = \varepsilon_k \tag{22}$$

where $R_G$ is the Gaussian radius, an adequate approximation of the Earth radius

$$R_G = \frac{a^2 \cdot b}{(a \cdot \cos\varphi_1)^2 + (b \cdot \sin\varphi_1)^2} \tag{23}$$

with $a$ and $b$ as the semi-axes of the reference ellipsoid (e.g. GRS80). The z-axis connects the geocenter with the starting point, the y-axis is defined perpendicular to the z-axis in direction (azimuth angle) of the GNSS satellite in view. After setting the initial parameters, the 'true' ray path is reconstructed iteratively ~~within two nested loops. In the *outer loop*, the meteorological parameters or total refractivity fields~~ by making use of ray-tracing shooting techniques. Therefore, total refractivity derived from an a priori field ~~are~~ is read in and pre-processed for ~~the inner loop. Therefore~~ray-tracing. Hereby, the input data is interpolated vertically and horizontally to the vertical plane, spanned by the y- and z-axis. ~~In the~~

In the ~~*inner*~~ *ray-tracing loop*, for each height layer $h_{i+1}$ with $i = 1 : (t-1)$ ~~where~~ whereby $t$ defines the top layer of the voxel model, the geocentric coordinates and the corresponding angles are computed as follows:

$$y_{i+1} = y_i + d_i \cdot \cos\varepsilon_i \tag{24}$$

$$z_{i+1} = z_i + d_i \cdot \sin\varepsilon_i \tag{25}$$

$$\eta_{i+1} = \arctan\frac{y_{i+1}}{z_{i+1}} \tag{26}$$

$$\theta_{i+1} = \arccos\left(\frac{n_i}{n_{i+1}} \cdot \cos(\theta_i + \eta_{i+1} - \eta_i)\right) \tag{27}$$

$$d_i = -(R_G + h_i) \cdot \sin\theta_i + \sqrt{(R_G + h_{i+1})^2 - (R_G + h_i)^2 \cdot \cos^2\theta_i} \tag{28}$$

$$\varepsilon_{i+1} = \theta_{i+1} - \eta_{i+1} \tag{29}$$

where $d_i$ is the reconstructed path length between height layer $h_i$ and $h_{i+1}$ $(h_{i+1} > h_i)$. It depends on the observation geometry but also on the atmospheric conditions (refractive indices $n_i$ and $n_{i+1}$). By default, for our analysis, the spacing between two height layers $h_i$ and $h_{i+1}$ was set to 5 m, which corresponds to a maximum path length $d_i$ of 100 m - assuming an ~~outgoing~~ elevation angle of 3° $(5m/sin3°)$. ~~The inner loop is repeated until~~

The ray-tracing loop stops when the ray reaches the top layer $t$ of the voxel model. Assuming spherical trigonometry, the spherical coordinates $(\varphi_{i+1}, \lambda_{i+1})$ of the ray path segments follow by Eqs. (24) and (25) to:

$$\varphi_{i+1} = \arcsin\Big(\sin\varphi_1 \cdot \cos(\eta_{i+1} - \eta_1) + \cos\varphi_1 \cdot \sin(\eta_{i+1} - \eta_1) \cdot \cos\alpha\Big) \tag{30}$$

$$\lambda_{i+1} = \lambda_1 + \arctan\left(\frac{\sin\alpha}{\cot(\eta_{i+1} - \eta_1) \cdot \cos\varphi_1 - \sin\varphi_1 \cdot \cos\alpha}\right) \tag{31}$$

where $\varphi_{i+1}$ and $\lambda_{i+1}$ are defined in the range $[-\pi/2, \pi/2]$ and $[-\pi, \pi]$, respectively. The ray coordinates are necessary for interpolation of the ~~a priori~~ refractive indices $n_i$ and $n_{i+1}$ for the next processing step $i$ but also for computation of the intersection points with the voxel model boundaries.

The ~~inner~~ ray-tracing loop is repeated until $\varepsilon_t - \varepsilon_k + g_{bend}$ is smaller than a predefined threshold (e.g. $10^{-6}$ degrees). While the elevation angle $\varepsilon_t$ is obtained by Eq. (~~23~~29) for $i = t-1$, the correction term $g_{bend}$ accounts for the additional bending above the ~~top layer of the~~ voxel model. Since atmosphere is almost in state of hydrostatic equilibrium, $g_{bend}$ can be well approximated by a bending model, like the one of Hobiger et al. (2008):

$$g_{bend}[°] = \frac{0.02 \cdot \exp^{\frac{-h}{6000}}}{\tan\varepsilon_k} \tag{32}$$

where $h$ is replaced by ~~the height~~ $h_t$, the height of the voxel top layer. After convergence of the ~~inner~~ ray-tracing loop, the path length in each voxel is obtained by summing up the distances $d_i$ in each voxel. Thereby, allocation of the ray parts is carried out by comparison of the ray coordinates $(\varphi_i, \lambda_i, h_i)$ with the coordinates of the voxel model. The obtained ray paths in each voxel - for each station and each satellite in view - are used for setting up design matrix $\boldsymbol{A}$ (see Eq. ~~5~~12).

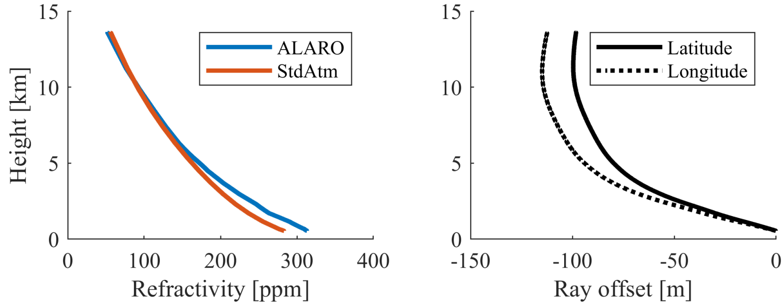


**Figure 2.** Ray-traced signal path differences (right) caused by differences in the a priori refractivity field (left)

## 4.2 Quality of reconstructed ray paths

### 4.2.1 The ~~a priori~~ refractivity field

The quality of the ray-traced signal paths depends primarily on the quality of the ~~a priori~~ refractivity field. Especially if no good a priori data can be made available, e.g. if standard atmosphere (StdAtm) is used instead of numerical weather model data (ALARO), the reconstructed signal path might deviate significantly from the 'true' signal path.

Figure 2 shows the impact of the ~~a priori~~ refractivity field on the signal ~~path~~geometry, exemplary for a GNSS signal observed at station Jenbach, Austria $(\varphi = 47.4°, \lambda = 11.8°, h = 545m)$ ~~at an elevation angle of 5°~~with $\varepsilon = 5°$ and $\alpha = 230°$. At this particular epoch (May 4, 2013, 15 UTC), standard atmosphere deviates by about 30 ppm from the ALARO model data. Assuming ~~that the ALARO data is correct~~ALARO as reference, ray-tracing through standard atmosphere causes a ray deviation of 100-200 m (see Fig. 2, right). ~~In consequence, the reconstructed signal travels significantly apart from the observed signal. In~~

In order to reduce the impact of possible ~~a priori~~ refractivity errors on the reconstructed ~~ray-paths~~ ray paths and in further consequence on the tomography solution, ~~the tomography processing~~ ray-tracing was carried out iteratively~~, i. e. the first~~. Therefore, the refractivity field obtained ~~by solving Eq. (7) for $N_w$ is used as a priori field for~~ from the first tomography solution replaces the initial refractivity field for ray-tracing for the next iteration and so on. The processing is repeated until $N_w$ converges.

Figure 3 (left) shows the convergence behavior ~~for two tomography solutions, which differ only with respect to the a priori refractivity field. Hereby, bias and~~ assuming standard atmosphere (StdAtm) and ALARO model data as input. In both cases, the standard deviation of the differences in ~~$N_w$~~ path length between two consecutive ~~solutions were~~ epochs ( $d_{k,i+1} - d_{k,i}$) was selected as convergence criteria. ~~In case of good a priori data, two iterationsare usually sufficient for $1ppm$-accuracy. Otherwise, e.g. when using standard atmosphere as a priori information, at least one iteration more is recommended. The adequate number of iterations depends also on the constraints applied to the a priori refractivity field. In case of too tight constraints, the number of iterations increases~~Both solutions converge after two iterations. Thereby, the path lengths within each voxel 'improve' by

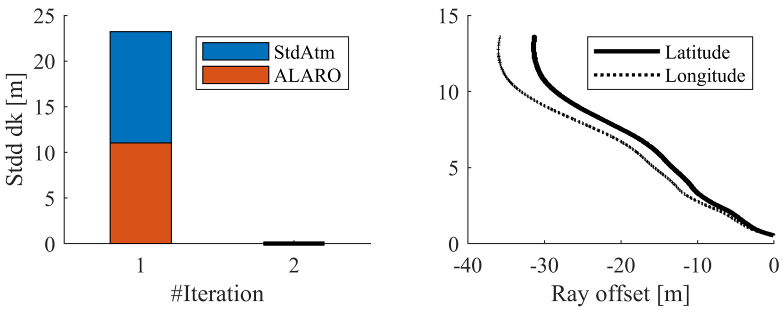


**Figure 3.** Convergence behavior (left) and ray-traced signal path differences after convergence (right). All iterations are based on the same first guess (standard atmosphere or ALARO numerical weather model data) but differ with respect to the refractivity field used for reconstruction of the bended signal paths

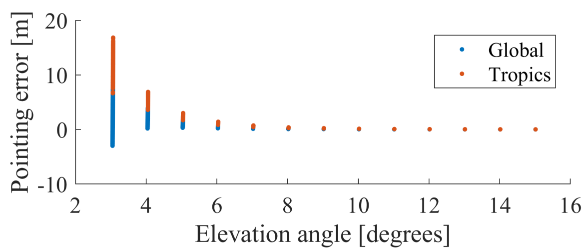


**Figure 4.** ~~Bias (left) and standard deviation (right) of~~ Point error at voxel model top ($h = 13.6km$) caused by the ~~differences in $N_w$ between two consecutive tomography solutions- calculated separately for standard atmosphere and ALARO numerical weather~~ bending model ~~data as~~ of Hobiger et al. (2008) - computed on a ~~priori refractivity field~~global $10°x10°$ grid over the period of one year, 2014 by comparison with ray-traced bending angles based on ECMWF analysis data

about $22m$ in case of standard atmosphere and by $11m$ in case of ALARO data. This result was expected, since ALARO data are closer to the 'true' atomospheric conditions. By comparison of Figure 3 (right) with Figure 2 (right) it is clearly visible, that the two additional iterations help to reduce the ray offset caused by errors in the standard atmosphere from $100-200m$ to $30-40m$. In Sect. 5 the resulting effect on the tomography solution is assessed.

#### 4.2.2 The empirical ray-bending model

Besides the ~~a priori~~ refractivity field, the quality of the reconstructed ray paths might be also affected by errors in the bending model ~~, see~~ as defined by Eq. (~~26~~32). Comparisons of the bending model with ray-traced bending angles on a global $10°x10°$ grid over the period of one year reveal that the error in bending is usually kept below 0.8 arcsec~~, see Fig. 4.~~. Assuming a GNSS site near sea-level and an elevation angle of $5°$, an error in bending angle of $\pm 0.8$ arcsec causes an error in path length of up to $\pm 10m$, i.e. the reconstructed GNSS signal enters the voxel model slightly earlier or later than the observed GNSS signal. In

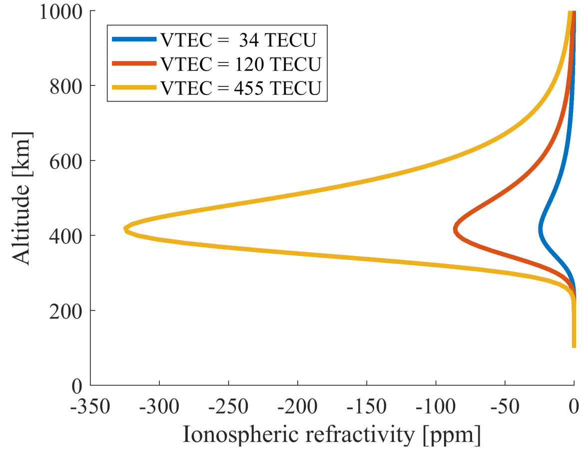


**Figure 5.** Profiles of ionospheric refractivity $N(f)$ assuming signal-frequency $f = 1575.42MHz$

Fig. 4, the bending error is visualized as pointing error at voxel model top. However, for the tomography solution this effect is too small to be significant. ~~In consequence,~~ Thus, it can be concluded that the bending model of Hobiger et al. (2008) is well applicable for reconstruction of the bending angle above the voxel model, in particular if the voxel model height $h_t$ is set to 12 km or higher. ~~Error in bending angle caused by the bending model of Hobiger et al. (2008) for $h = 12km$ (above the voxel model) - computed on a global $10° x 10°$ grid over the period of one year, 2014 by comparison with ray-traced bending angles based on ECMWF analysis data~~

#### 4.2.3 Ionospheric bending effects

Beyond, also the ionosphere influences GNSS signal propagation. In order to assess the impact of free electrons in the ionosphere (above 80 km altitude) on the signal path, the electron density model by Anderson et al. (1987) was executed in three scenarios, assuming a vertical total electron content ($VTEC = \int N_e \cdot dh$) of 34 TECU (average daytime), 120 TECU (solar maximum) and 455 TECU (maximum possible, see Wijaya, 2010), respectively.

$$N(f) = 10^6 \cdot \frac{-40.2993 \cdot N_e}{f^2} \tag{33}$$

By making use of Eq. (~~27~~33), the obtained electron density profiles were converted into profiles of refractivity (N), assuming signal frequency $f_1 = 1575.42MHz$ (GPS L1) and $f_2 = 1227.60MHz$ (GPS L2). Figure 5 shows the obtained vertical profiles of ionospheric refractivity, exemplary for frequency $f_1$. The higher the signal-frequency $f$ the lower the phase velocity through the ionosphere and the less is its refraction. Following the approach by Wijaya (2010), the ray paths in the ionosphere were reconstructed, separately for GPS L1 and L2. The analysis revealed significant path differences between the 'true' ray path and its chord line but also between the two signal-frequencies. Assuming a VTEC of 455 TECU and an elevation angle of 3°, the maximum deviation from the ~~straight-line~~ straight line signal path is 800 m for L1 and 550 m for L2 respectively, at $h = 400km$, slightly below the layer of peak electron density. Fortunately, ray path deviation decreases significantly with decreasing VTEC and altitude to a few tens of meters at ~~$h = 12km$~~ $h = 13.6km$ (the upper rim of the troposphere at which the top of the voxel model ~~is usually~~ was defined). In consequence, the impact of free electrons on the signal path in the lower atmosphere is negligible under moderate and low ionospheric conditions. ~~Profiles of ionospheric refractivity $N(f)$ assuming signal-frequency $f = 1575.42 MHz$~~

## 5 Impact of atmospheric bending on the tomography solution

In the following, the differences between straight line and bended ray-tracing are further analyzed. For highest consistency, the ray-tracing approach defined in Sect. ~~3~~ 4 was used for both, straight line and bended ray-tracing. The only difference is that in case of straight line ray-tracing the ratio $n_i/n_{i+1}$ in Eq. (~~21~~27) was set to '1'. Thereby, it can be guaranteed that only the impact of atmospheric refraction is assessed.

### 5.1 Expected drying effect

In the beginning, the ray position is equal for both methods but diverges with increasing height. Thereby, the bended ray is travelling in most cases 'above' the straight ray, i.e. the straight ray enters the voxel model top 'earlier' than the bended ray. This leads to the effect that the straight ray remains longer in the voxel model than the bended ray, i.e. the straight ray path within the voxel model $(h < 13.6km)$ is systematically longer than the bended ray path. The differences between both ray paths are plotted in Fig. 6 (top) as function of elevation angle. Therefore, ALARO model data was selected as input for the bended ray-tracer.

The additional ray path decreases rapidly with increasing elevation angle. Thus, a *mixed ray-tracing* approach can be defined, which considers ray bending only for $\varepsilon \leq 15°$. Beyond, the additional ray path is below 0.1 km, and straight line ray-tracing is sufficient for ray path reconstruction.

Figure 6 (top) shows also that in some cases even for low elevation angles the difference in path length is small (below 0.1 km). This appears when the ray enters the voxel model not through the top layer but through a later surface of the voxel model. In this particular case, the difference in path length between both ray-tracing approaches is negligible (be aware that only the entire distance through all voxels is comparable for both ray-tracing approaches but not the individual distances in each voxel). Figure 6 (bottom) shows the expected drying effects in the tomography solution caused by errors in the reconstructed signal paths assuming straight line geometry. Hereby, it is distinguished between the drying effect caused by the additional ray path $(dNw_1)$ and the drying effect caused by the fact that the straight line travels through lower layers of the voxel model $(dNw_2)$. Both effects were assessed as follows:

$$dNw_1 = SWD_b \cdot (d_{k,s} - d_{k,b}) \quad (34)$$

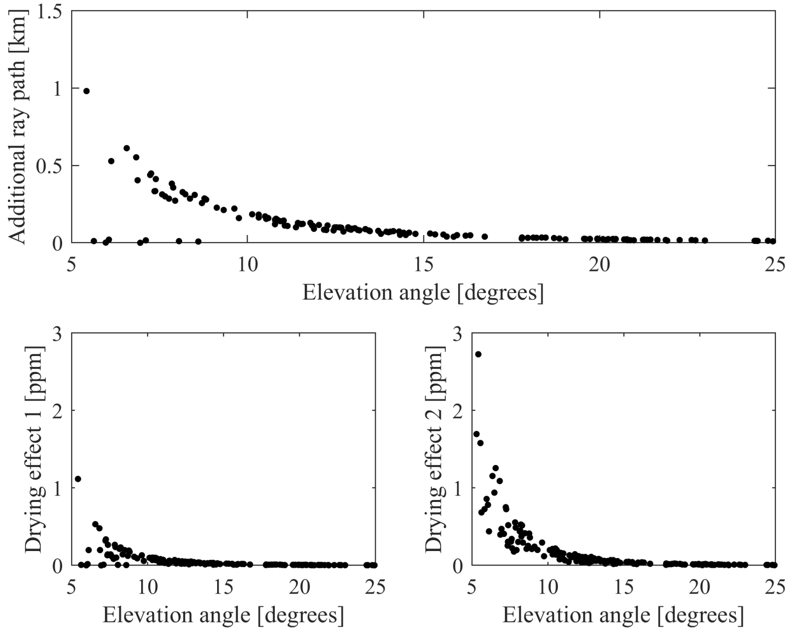


**Figure 6.** Additional ray path caused by straight line ~~ray-tracing~~assumption (top), the resulting drying effect due to the additional ray path (bottom left) and the resulting drying effect caused by the fact that the straight line ray travels through lower atmospheric levels than the 'true' bended ray (bottom right)

$$dNw_2 = (SWD_b - SWD_s) \cdot d_{k,s} \tag{35}$$

whereby $SWD_b$ and $SWD_s$ are the slant wet delays obtained by ray-tracing through ALARO model data along the bended and the straight line ray path, respectively. The variables $d_{k,b}$ and $d_{k,s}$ are the corresponding path lengths within the voxel model. The sum of their differences along the ray paths are identical with the additional ray paths plotted in Figure 6 (top).

Both drying effects have to be considered as additive and are strongly connected to the current atmospheric conditions as well as to the parametrization applied for interpolation of the refractivity field. In our analysis we assumed an exponential decrease of refractivity between the vertical layers of the voxel model and applied a bi-linear interpolation method for horizontal interpolation between the grid points.

### 5.2 Results from the Austrian GNSS tomography test case

In order to study the impact of bended ray-tracing on the tomography solution, a GNSS tomography test case was defined. The corresponding settings are summarized in Table 1.

**Table 1.** Summary of GNSS tomography test case settings

| Parameter | Settings |
|---|---|
| Period | May 2013, 8 epochs per day |
| Voxel domain | Western Austria ($46.4-48.0°$ lat, $10.4-13.4°$ lon, h = $0-13.6km$) |
| Voxel size | $0.4°$ lat x $0.6°$ lon (4 x 5 ground voxels), 15 height layers |
| GNSS data | 30 sec dual-frequency GPS and GLONASS observations - obtained from 6 EPOSA reference sites: SEEF, MATR, JENB, KIBG, ROET, SILL |
| A priori model | ALARO analysis data of temperature and specific humidity - provided on 18 pressure levels in grib1 format for 8 epochs per day |
| Observations | SWDs for all GPS and GLONASS satellites in view above $3°$ elevation angle - derived from 1h ZTD and 2h gradient estimates |
| Ray-tracer | Sol1: Straight line ray-tracing for all observations up to $h = 13.6km$ Sol2: Straight line ray-tracing for $\varepsilon > 15°$ and bended ray-tracing for $\varepsilon \leq 15°$ (mixed approach) up to $h = 13.6km$ |

Figure 7 (left) shows the differences in wet refractivity ~~obtained for the GNSS tomography test case on May 4, 2013, 15 UTC, whereby voxel number '~~between Sol1 and Sol2 (as defined in Table 1~~' is dedicated to the South-West corner and number '20' to the North-East corner of the voxel model. Between the voxels a bilinear interpolation method was applied.~~). Even though on average over all voxels no bias in wet refractivity is observed, specific voxels show differences in wet refractivity of up to ~~12 ppm~~$10ppm$, particularly if due to bending different voxels than in the straight line solution are traversed.

Figure 7 (right) shows the differences in wet refractivity between ~~two consecutive tomography solutions based on~~ the first two iterations of the mixed ray-tracing approach (Sol2~~, see Table 1). For Figure 7 (left) the a priori model was replaced by the improved wet refractivity field of the first solution (iterative solution).~~). In this particular case, refractivity differences ~~of up to 0.5 ppm are visible~~ are smaller than $0.05ppm$, which implies that the a priori model used for ~~the first solution~~ ray-tracing is already close to the 'true' atmospheric conditions, i.e. in this particular case no further iteration was necessary. From all differences in wet refractivity over 248 epochs in May 2013, a maximum of ~~$15.6ppm$~~$14.2ppm$, a bias of ~~$0.08ppm$~~ $0.12ppm$ and a standard deviation of ~~$0.2ppm$~~ $0.24ppm$ were obtained. Although the bias and standard deviation over all voxels is small, differences of about $1ppm$ were observed on average at each epoch, especially when observations below ~~$10°$~~ 10 degrees elevation angle enter the tomography solution.

### 5.3 Validation with radiosonde data

For validation of the mixed ray-tracing approach against straight line ray-tracing, the tomography derived wet refractivity fields were compared with radiosonde data at the airport of Innsbruck ($\varphi_i = 47.3°, \lambda = 11.4°, h = 579m$). First, the radiosonde data obtained once a day between 2 and 3 UTC were pre-processed, i.e. outliers in temperature were removed and dew point tem-

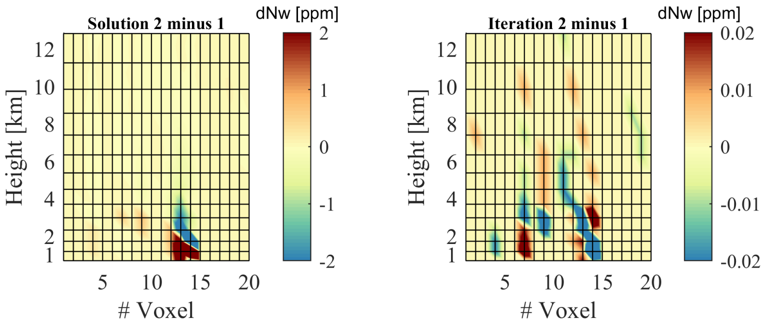


**Figure 7.** ~~(left): Differences~~ Error in wet refractivity ~~between~~ caused by straight line ~~and mixed straight line / bended ray-tracing solution,~~ assumption (~~right~~left) ~~: Differences~~ and the differences in wet refractivity between first and second iteration (~~compare also~~ right). Thereby, voxel number '1' is dedicated to ~~Fig~~the South-West corner and number '20' to the North-East corner of the voxel model. ~~3)~~For visualization, a bi-linear interpolation method was applied between the grid points. Analyzed period: May 4, 2013, 15 UTC

perature was converted to water vapor pressure and further to wet refractivity. Finally, the radiosonde profiles were vertically interpolated to the height layers of the voxel model and the tomography derived wet refractivity fields were horizontally interpolated to the ground-position of the radiosonde launching site, respectively. Figure 8 shows the differences in wet refractivity as function of height above surface, exemplarily for two epochs in May, 2013. In both cases, the bended ray-tracing approach helps to reduce the tomography error by about $1-2ppm$, especially in the lower 4 km of the atmosphere. Largest differences are visible when the bended ray traverses other voxels than its chord line. This appeared in about 2 % of the test cases, especially if observations below ~~10°~~ 10 degrees elevation angle enter the tomography solution.

## 6 Conclusions

GNSS signals which enter the neutral atmosphere at low elevation angles ~~($\varepsilon < 15°$)~~ ($\varepsilon$ < 15 degrees) are significantly affected by atmospheric bending. In case the bending is neglected when setting up design matrix $\boldsymbol{A}$, a systematic error of up to $10-20ppm$, on average of $1-2ppm$ is introduced into the GNSS tomography solution. This error can be widely reduced if atmospheric bending is considered in reconstruction of the signal paths. Therefore, a 2D piecewise linear ray-tracing approach ~~has been~~ was defined, which describes the bended GNSS signal path by small line segments. By limiting the length of the line segments to $100m$ in case of $\varepsilon = 3°$ or even shorter for higher elevation angles, the 'true' signal path can be widely reconstructed. However, the quality of the reconstructed signal paths depends primarily on the quality of the a priori refractivity field. Comparisons between refractivity fields derived from standard atmosphere and ALARO weather model data reveal that ~~an a priori~~ a refractivity error of $30ppm$ can cause a ray deviation of up to several hundred meters, i.e. the distance traveled in each voxel but also the number of traversed voxels is prone to misallocations. In consequence, reliable a priori data, e.g. derived from numerical weather model data, are recommended for GNSS tomography.

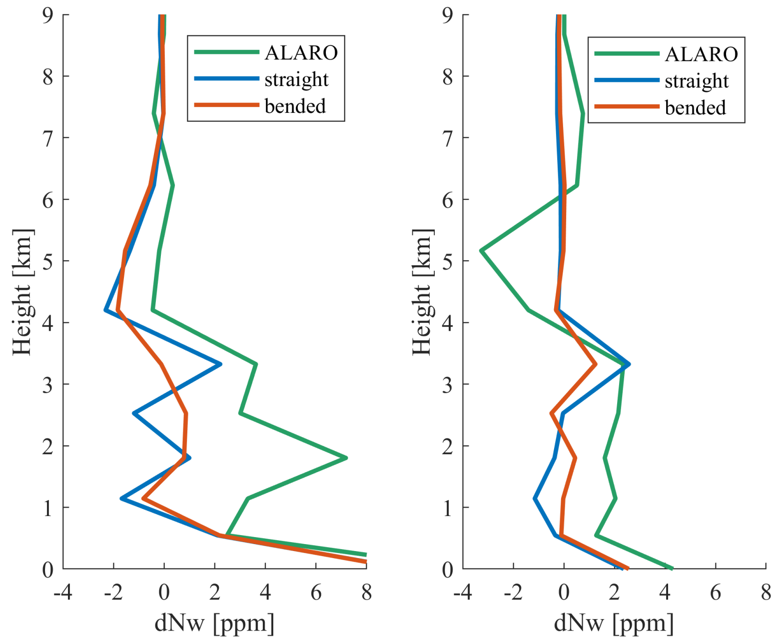


**Figure 8.** Differences in wet refractivity between radiosonde, ALARO and the two tomography solutions based on straight line (blue) and bended ray-tracing (red), exemplary for May 1, 2013, 3 UTC (left) and May 31, 3 UTC (right)

Nevertheless, if reliable a priori data are not available or if the quality is unknown, iterative ~~tomography processing~~ ray-tracing helps for reducing the impact of ~~the a priori refractivity field~~ wet refractivity errors on the tomography solution. Therefore, the wet refractivity field obtained from an initial tomography solution is ~~introduced as a priori information for the~~ used for reconstruction of the signal paths for the next iteration. The processing is repeated until the tomography solution converges. This ensues usually after ~~2-3 iterations- dependent on the quality of the a priori data and whether constraints are applied to the a priori field. Thereby~~two iterations. Beyond, a bending model, like the one provided by Hobiger et al. (2008) helps to significantly reduce computational cost by describing the remaining bending in the higher atmosphere (above the voxel model). In consequence, the ray-tracer can be stopped right after the reconstructed signal leaves the voxel model. In case of $\cancel{h_t = 12km}$$h_t = 13.6km$, the number of processing steps is reduced by $85\%$, which is a tremendous reduction in processing time without significant loss of accuracy.

In contrast, ionospheric bending effects have less impact on the GNSS tomography solution. Even during periods of solar maximum, ray path deviation caused by ionospheric bending is negligible for signals in L-band $(1-2GHz)$. However, even if ionospheric bending has no impact on the tomography solution, first and higher order ionospheric effects should be taken into account when processing GNSS phase observations.

Besides, comparisons with radiosonde data revealed that if atmospheric bending effects are considered in GNSS tomography, the quality of the tomography solution can be improved by $1-2ppm$. Within the defined test case, especially voxels in the lower $4km$ of the atmosphere benefitted from the applied mixed ray-tracing approach. Due to significant optimization, the mixed ray-tracing approach ensures processing of large tomography test cases in adequate time. A test case with 72 GNSS sites and 7 x 9 x 15 voxels can be processed in less than two minutes. Thus, the developed mixed ray-tracing approach is applicable also in near real-time and therefore well suited for operational purposes.

*Code availability.* The 2D piecewise linear ray-tracer for GNSS tomography as well as the RADIATE ray-tracer are part of the Vienna VLBI and Satellite Software (VieVS). The code of the RADIATE ray-tracer is available at https://github.com/TUW-VieVS/RADIATE. For more details to VieVS, the reader is referred to http://vievswiki.geo.tuwien.ac.at.

## Appendix A: Unmodelled bending effects in the Vienna hydrostatic mapping function

In case of VMF1 (Böhm et al., 2006) or similar mapping concepts, azimuthal asymmetry is not considered and for convenience, only a single hydrostatic mapping coefficient per site $(a_h)$ is determined as follows:

$$a_h = -\frac{mf_h(\varepsilon) \cdot \sin\varepsilon - 1}{\frac{mf_h(\varepsilon)}{\sin\varepsilon + \frac{b_h}{\sin\varepsilon + c_h}} - \frac{1}{1+\frac{b_h}{1+c_h}}}. \tag{A1}$$

where $b_h$ is 0.0029, $c_h$ depends on the day of year and latitude and $mf_h(\varepsilon)$ is defined as the ratio between $SHD(3°)$ and $ZHD$, obtained by ray-tracing through numerical weather model data. For assessing the remaining unmodeled geometric bending $dg_{bend}(\varepsilon,\alpha)$, ray-traced slant hydrostatic delays were compared with 'mapped' slant hydrostatic delays as follows:

$$dg_{bend}(\varepsilon,\alpha)[m] = ZHD[m] \cdot mf_h(\varepsilon) - ZHD[m] \cdot mf_{h0}(\varepsilon) - g_{bend}(\varepsilon,\alpha)[m] \tag{A2}$$

where $ZHD$ is the zenith hydrostatic delay obtained by vertical integration, $g_{bend}(\varepsilon,\alpha)$ is the geometric bending effect as obtained by ray-tracing, $mf_h(\varepsilon)$ is the VMF1 hydrostatic mapping function determined by $SHD(3°)/ZHD$ and $mf_{h0}(\varepsilon)$ is the hydrostatic mapping function determined by $SHD_0(3°)/ZHD$, whereby $SHD(3°)$ and $SHD_0(3°)$ are the slant hydrostatic delays obtained by ray-tracing for an ~~outgoing~~ vacuum elevation angle $\varepsilon_k = 3°$ with and without geometric bending, respectively. Figure A1 shows the remaining unmodeled geometric bending as obtained for six elevation angles (and 16 equidistant azimuth angles), exemplary for the two VLBI sites Fortaleza, Brazil $(\varphi = -3.9°, \lambda = 321.6°, h = 23m)$ and Wettzell, Germany $(\varphi = 49.1°, \lambda = 12.9°, h = 669m)$. In case of $\varepsilon = 3°$, almost no bending error is visible since $mf_h(\varepsilon)$ was tuned for this elevation angle. However, for other elevation angles, the unmodeled geometric bending is about 3 % of the slant hydrostatic delay, e.g. up to $\pm 5mm$ at 5° elevation angle. In case of Wettzell, $dg_{bend}(\varepsilon,\alpha)$ is mostly negative, i.e. the 'mapped' $SHD$ is smaller than the observed $SHD$ and vice versa for Fortaleza. So far, these small variations are neglected when using VMF1 hydrostatic mapping function in GNSS signal processing.

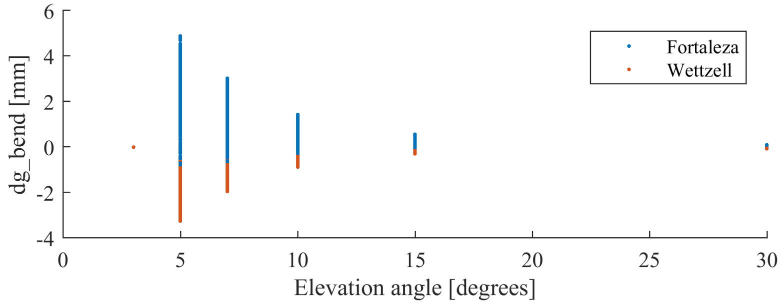


**Figure A1.** The unmodeled geometric bending effect in VMF1 hydrostatic mapping function ($dg_{bend}$), exemplary for VLBI sites Fortaleza, Brazil and Wettzell, Germany. Analyzed period: Jan-Feb 2014

*Acknowledgements.* Open access funding was provided by Austrian Science Fund (FWF). The authors would like to thank the Austrian Science Fund (FWF) for financial support of this study within the project RADIATE ORD (ORD 86) and the Austrian Research Promotion Agency (FFG) for finacial support within the project GNSS-ATom (840098).

## References


Aghajany, S. H. and Amerian, Y.: Three dimensional ray tracing technique for tropospheric water vapor tomography using GPS measurements, J. Atmospheric Sol.-Terr. Phys., 164, 81–88, https://doi.org/10.1016/j.jastp.2017.08.003, 2017.

Anderson, D. N., Mendillo, M., and Herniter, B.: A semi-empirical low-latitude ionospheric model, Radio Sci., 22, 292–306, https://doi.org/10.1029/RS022i002p00292, 1987.

Bender, M. and Raabe, A.: Preconditions to ground based GPS water vapour tomography, Ann. Geophys., 25, 1727–1734, https://doi.org/10.5194/angeo-25-1727-2007, 2007.

Bender, M., Stosius, R., Zus, F., Dick, G., Wickert, J., and Raabe, A.: GNSS water vapour tomography - Expected improvements by combining GPS, GLONASS and Galileo observations, Adv. Space Res., 47, 886–897, https://doi.org/10.1016/j.asr.2010.09.011, 2011.

Bevis, M., Businger, S., Herring, T. A., Rocken, C., Anthes, R. A., and Ware, R. H.: GPS meteorology: Remote sensing of atmospheric water vapor using the Global Positioning System, J. Geophys. Res., 97, 15 787–15 801, https://doi.org/10.1029/92JD01517, 1992.

Böhm, J., Werl, B., and Schuh, H.: Troposphere mapping functions for GPS and Very Long Baseline Interferometry from European Centre for Medium-Range Weather Forecasts operational analysis data, J. Geophys. Res., 111, 1–9, https://doi.org/10.1029/2005JB003629, 2006.

Champollion, C., Masson, F., Bouin, M.-N., Walpersdorf, A., Doerflinger, E., Bock, O., and Bealen, J. V.: GPS water vapour tomography: preliminary results from the ESCOMPTE field experiment, Atm. Res., 74, 253–274, https://doi.org/10.1016/j.atmosres.2004.04.003, 2005.

Chen, G. and Herring, T. A.: Effects of atmospheric azimuthal asymmetry on the analysis of space geodetic data, J. Geophys. Res., 102, 20 489–20 502, https://doi.org/10.1029/97JB01739, 1997.

Flores Jimenez, A.: Atmospheric tomography using satellite radio signals, Ph.D. thesis, Universitat Politecnica de Catalunya, Departament de Teoria del Senyal i Comunicacions, http://www.tdx.cat/handle/10803/6881, 1999.

Fritsche, M., Dietrich, R., Knöfel, C., Rülke, A., Vey, S., Rothacher, M., and Steigenberger, P.: Impact of higher-order ionospheric terms on GPS estimates, J. Geophys. Res., 32, 1–5, https://doi.org/10.1029/2005GL024342, 2005.

Hansen, P. C.: The L-curve and its use in the numerical treatment of inverse problems, in: Computational Inverse Problems in Electrocardiology, Advances in Computational Bioengineering, ISBN: 1853126144, pp. 119–142, WIT Press, 2000.

Hirahara, K.: Local GPS tropospheric tomography, Earth Planets Space, 52, 935–939, https://doi.org/10.1186/BF03352308, 2000.

Hobiger, T., Ichikawa, R., Koyama, Y., and Kondo, T.: Fast and accurate ray-tracing algorithms for real-time space geodetic applications using numerical weather models, J. Geophys. Res., 113, 1–14, https://doi.org/10.1029/2008JD010503, 2008.

Hofmeister, A.: Determination of path delays in the atmosphere for geodetic VLBI by means of ray-tracing, Ph.D. thesis, TU Wien, Department of Geodesy and Geoinformation, http://repositum.tuwien.ac.at/obvutwhs/content/titleinfo/1370367, 2016.

Iyer, H. M. and Hirahara, K.: Seismic tomography: Theory and practice, Springer Netherlands, iSBN: 0412371901, 1993.

Kruse, L. P.: Spatial and Temporal Distribution of Atmospheric Water Vapor using Space Geodetic Techniques, Geodätisch-geophysikalische Arbeiten in der Schweiz, 61, 2001.

Landskron, D. and Böhm, J.: Refined discrete and empirical horizontal gradients in VLBI analysis, J. Geod., 92, 1387–1399, https://doi.org/10.1007/s00190-018-1127-1, 2018.

MacMillan, D. S.: Atmospheric gradients from Very Long Baseline Interferometry observations, Geophys. Res. Lett., 22, 1041–1044, https://doi.org/10.1029/95GL00887, 1995.

Manning, T.: Sensing the dynamics of severe weather using 4D GPS tomography in the Australien region, Ph.D. thesis, Royal Melbourne Institute of Technology, School of Mathematical and Geospatial Sciences, http://researchbank.rmit.edu.au/eserv/rmit:160752/Manning.pdf, 2013.

Möller, G.: Reconstruction of 3D wet refractivity fields in the lower atmosphere along bended GNSS signal paths, Ph.D. thesis, TU Wien, Department of Geodesy and Geoinformation, http://repositum.tuwien.ac.at/obvutwhs/content/titleinfo/2268559, 2017.

Nievinski, F. G.: Ray-tracing to mitigate the neutral atmosphere delay in GPS, Master's thesis, University of New Brunswick, Department of Geodesy and Geomatics Engineering, http://www2.unb.ca/gge/Pubs/TR262.pdf, 2009.

Nilsson, T.: Assessment of tomographic methods for estimation of atmospheric water vapor using ground-based GPS, Ph.D. thesis, Chalmers University of Technology, Göteborg, Department of Radio and Space Science, Sweden, 2005.

Raymond, T. D., Franke, S. J., and Yeh, K. C.: Ionospheric tomography: its limitations and reconstruction methods, J. Atmospheric Terr. Phys., 56, 637–657, https://doi.org/10.1016/0021-9169(94)90104-X, 1994.

Steiner, A. K., Löscher, A., and Kirchengast, G.: Error characteristics of Refractivity Profiles Retrieved from CHAMP Radio Occultation Data, pp. 27–36, Springer Berlin Heidelberg, Atmosphere and Climate: Studies by Occultation Methods, https://doi.org/10.1007/3-540-34121-8_3, 2006.

Wijaya, D. D.: Atmospheric correction formulae for space geodetic techniques, Ph.D. thesis, Graz University of Technology, Faculty of Technical Mathematics and Technical Physics, http://www.shaker.de/Online-Gesamtkatalog-Download/2018.11.26-19.55.57-207.151.220.142-rad6E460.tmp/3-8322-8994-1_INH.PDF, 2010.

Zou, X., Vandenberghe, F., Wang, B., Gorbunov, M. E., Kuo, Y., Sokolovskiy, S., Chang, J. C., Sela, J. G., and Anthes, R. A.: A ray-tracing operator and its adjoint for the use of GPS/MET refraction angle measurements, J. Geophys. Res.: Atmospheres, 104, 22 301–22 318, https://doi.org/10.1029/1999JD900450, 1999.

Zus, F., Dick, G., Heise, S., and Wickert, J.: A forward operator and its adjoint for GPS slant total delays, Radio Sci., 50, 393–405, https://doi.org/10.1002/2014RS005584, 2015.

~~al (one-way) chemical reactions~~